LASER INTERFEROMETER GRAVITATIONAL WAVE OBSERVATORY
- LIGO -
CALIFORNIA INSTITUTE OF TECHNOLOGY
MASSACHUSETTS INSTITUTE OF TECHNOLOGY

Publication	LIGO-P1500190–v1	2015/09/27

Assessing the Merit of a Space-Based Gravitational Wave Antenna for Cosmography and Black Hole Spectroscopy

Jared Goldberg, Tom Callister, Rana Adhikari, Curt Cutler

California Institute of Technology
LIGO Project, MS 18-34
Pasadena, CA 91125
Phone (626) 395-2129
Fax (626) 304-9834
E-mail: info@ligo.caltech.edu

Massachusetts Institute of Technology
LIGO Project, Room NW22-295
Cambridge, MA 02139
Phone (617) 253-4824
Fax (617) 253-7014
E-mail: info@ligo.mit.edu

LIGO Hanford Observatory
Route 10, Mile Marker 2
Richland, WA 99352
Phone (509) 372-8106
Fax (509) 372-8137
E-mail: info@ligo.caltech.edu

LIGO Livingston Observatory
19100 LIGO Lane
Livingston, LA 70754
Phone (225) 686-3100
Fax (225) 686-7189
E-mail: info@ligo.caltech.edu

http://www.ligo.caltech.edu/

1 Abstract

Physicists are creating a network of gravitational wave (GW) detectors on Earth that will be capable of detecting GW signals from low-mass compact binary systems. In order to observe more massive binaries, which coalesce at frequencies inaccessible to ground-based detectors due to seismic noise, plans have also been made to create space-based detectors. However, the most serious of these proposals, LISA, is not scheduled for launch until 2034 due to its extreme cost. Therefore, recent efforts have aimed at designing lower-cost detectors that could span a similar frequency band. This project aims to evaluate the scientific merit of one such proposed space-based detector. The proposed detector is sensitive to GW signals in the range of $10^{-3}-10^{2}$ Hz, overlapping with the earth-based detectors. We calculate the detectors best-case signal-to-noise ratio as a function of a sources location and orientation, and using the Fisher Matrix formalism, we calculate how accurately the detector could locate sources in the sky. We find that, while the instrument can strongly detect GWs out to cosmological distances, its noise curve is too high to accurately pinpoint its sources at distant redshifts. However, upon synthesizing this detector's data with data from earth-based detectors, the detector may still be able to locate interesting GW sources.

2 Introduction and General Background

The theory of general relativity requires the existence of gravitational radiation in the form of waves in spacetime. If general relativity is correct, these gravitational waves (GWs) travel at the speed of light, carrying information about changing gravitational fields from accelerating massive objects. This kind of radiation can exist across a tremendous range of frequencies, ranging over orders of magnitude from 10^{-10} Hz, created by the expansion of the early universe and the motion of supermassive binary systems, up to 10^{3} Hz, typically caused by supernovae and rotating neutron stars [2]. Figure 1 shows the frequencies at which certain sources radiate and the relatives sensativities of current and planned GW detectors [10].

2.1 Ground-Based Detectors

Currently, physicists are working to create a network of gravitational wave detectors on Earth, which at present includes Advanced Virgo in Italy and two Advanced LIGO detectors in the United States, with detectors in the works in Japan and India [7]. These Earth-based detectors will be sensitive to gravitational waves at the higher end of the frequency range, from $10-10^{3}$ Hz, and will search for signals from sources such as the coalescence of compact binary black holes or neutron stars, supernovae, and pulsars (rotating neutron stars) [9]. These detectors, however, can only observe the final moments of only the lightest binary systems, since the frequency of a binary at its innermost stable circular orbit is [9]

$$f_{ISCO} = 2.2\text{kHz}\left(\frac{M_{\odot}}{M}\right) \tag{1}$$

where M is the binary's total mass, and it would be interesting and beneficial to observe

these systems much earlier in their evolution. Moreover, it would be useful to be able to observe the coalescence of more massive sources. Unfortunately, there is simply too much seismic noise to be able to observe these lower-frequency waves on Earth.

2.2 Space-Based Detectors

In order to observe GWs at lower frequencies, plans have been made to create space-based detectors, capable of detecting signals from more massive sources, since the frequency at which binaries merge varies inversely with their total mass. These sources include binary star systems and coalescing binary systems containing extreme mass ratios (one supermassive black hole and one stellar-mass body). One such proposed detector is LISA, a triangular configuration of satellites with arms a million kilometers in length (compared to LIGOs 4 km arms), which is designed to be sensitive over frequencies of $10^{-5} - 10^{-1}$ Hz [8]. However, due to its tremendous cost, it has been difficult to fund the project, and with NASAs withdrawal in 2011, LISA is not scheduled for launch by the ESA until the early 2030s [12]. Therefore, recent efforts have aimed at designing lower-cost alternatives to LISA that could span a similar frequency band, and thus could garner financial support for an earlier launch.

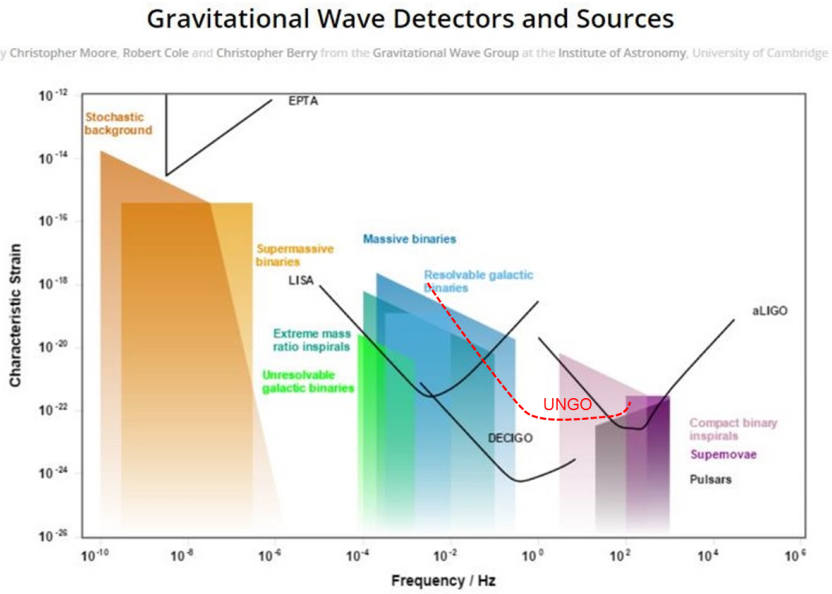

Figure 1: Frequencies emitted gravitational wave sources, and the sensitivity curves of the different types of GW detectors that detect them. The proposed UNGO detector curve is added in dashed red. Waves produced by sources lying above the detector curves are in principle detectable, whereas the waves produced by sources lying below the curves are too weak to detect.

3 Objectives

The UNGO mission (name subject to change) is one such project. The concept is, instead of a detector with 1 million km-long arms, to send a smaller LISA-like interferometer, with 2 laser arms of roughly 100 km, into orbit around the Sun. The proposed detector will have a 532 nm laser with a power of 20W, a telescope mirror diameter of 37.5 cm, and will utilize squeezed light to reduce noise. UNGO will be sensitive to gravitational waves somewhere between LISA's and aLIGOs frequency bands (similar to the Decigo band in Figure 1, $10^{-2} - 10^{2}$ Hz), and thus could give useful information about sources we could not detect from Earth (see Figures 1 and 2). For instance, we could detect more massive binaries composed of intermediate mass black holes, which are unlikely to be seen by LIGO. Additionally, UNGO could detect stellar-mass binaries (which eventually will enter the LIGO band) much earlier on in their orbital evolution, providing an early warning for both ground-based gravitational wave detectors and electromagnetic telescopes. This project will assess the scientific merit of such a concept, including the maximum theoretical signal-to-noise ratio with which it could detect gravitational wave sources, and the maximum accuracy with which it could determine information about its sources, such as mass, distance, orientation, and location.

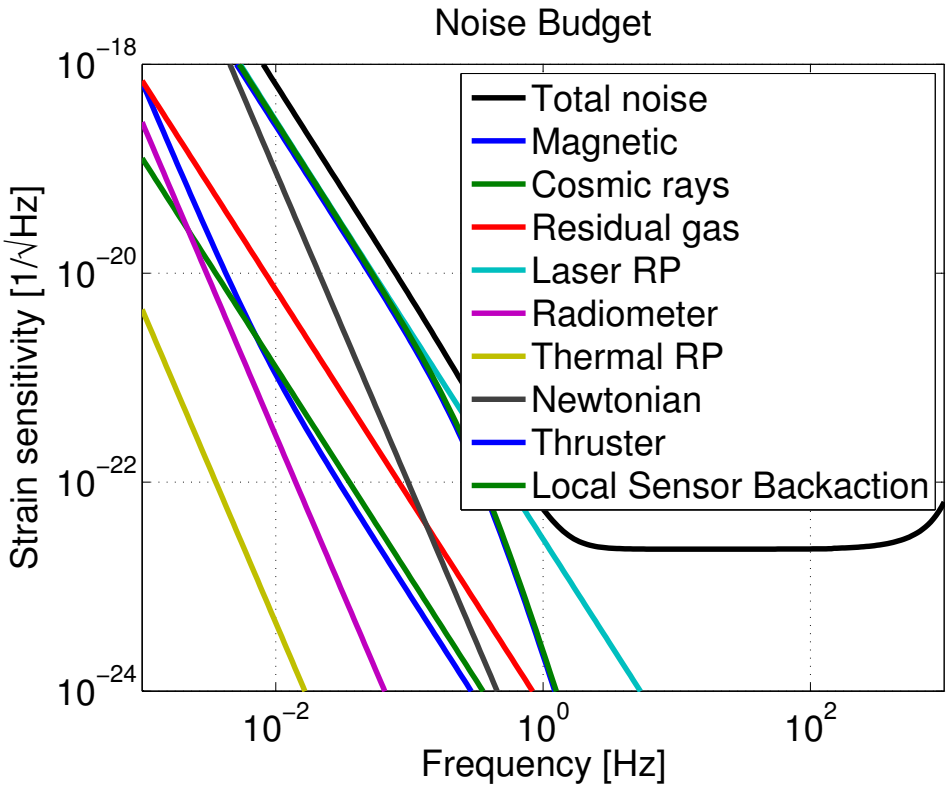

Figure 2: Sources of noise for UNGO, and the detector's sensitivity curve.

4 Methods

The sensitivity of a space-based gravitational wave detector is limited by several sources of noise. Noise can come from the instrument itself, due to temperature fluctuations, loss in sensitivity when the wavelength of the source approaches the length of the arms of the detector, and laser shot noise [2]. Professor Adhikari provided code to estimate the noise due to a wide variety of sources, and provided us with a noise curve (Figure 2).

With the noise budget computed, we then estimate the signal-to-noise ratio (SNR) with which UNGO will detect various gravitational wave sources. To calculate the projected signal to noise ratio, the basic equation is conveniently written as the inner product of the specified gravitational waveform with itself:

$$(\mathrm{SNR})^2 = (h|h), \tag{2}$$

where the inner product $(A|B)$ is defined by:

$$(A|B) = 4 \times \Re \int_0^\infty \frac{\tilde{A}^*(f)\,\tilde{B}(f)}{S_n(f)}\,\mathrm{d}f \tag{3}$$

where a tilde denotes the fourier transform of a quantity into the frequency domain. SNR is the optimal value of the signal-to-noise ratio, $h(f)$ is the GW signal, and $\mathrm{S_n}(f)$ is the power-spectral density of the detector, related to the level of detector noise [5].

Because the detector has noise, it is impossible to recover the exact correct parameters of the source. However, under certain circumstances and loud signals, it is possible to estimate the expected errors in parameter extractions by defining the Fisher Matrix, given by [6]

$$\Gamma^{\mu\nu} = \left(\frac{\partial h}{\partial \lambda^\mu}\middle|\frac{\partial h}{\partial \lambda^\nu}\right), \tag{4}$$

where λ^μ is the μth parameter, and $\frac{\partial h}{\partial \lambda^\mu}$ is the partial derivative of the waveform h with respect to that parameter. Invert this quantity, and the diagonals are the square of the single-parameter errors, and the off-diagonals are the covarience errors of the different parameters. That is, we calculate the expectation values of the errors in estimating different physical parameters by finding the covariance matrix:

$$\overline{\Delta\lambda^\mu \Delta\lambda^\nu} = (\Gamma^{-1})^{\mu\nu} \times (1 + \mathcal{O}(\mathrm{SNR})^{-1}). \tag{5}$$

We also compute the evolution of the frequency of the system with respect to time. This can, among other things, allow us to see how long an object will be able to stay within the detectors sensitivity band [9]. To a first approximation, the frequency evolves as

$$f(t) = \frac{134(1.21 M_\odot/\mathcal{M}_L)^{\frac{5}{8}}}{(t_c - t)^{\frac{3}{8}}}. \tag{6}$$

We do our analysis first considering a detector with an antenna pattern of just 2 arms, and then we look at a 3-arm pattern, looking at several test cases, including: neutron

star/ neutron star (1.5/1.4 $M_\odot$), neutron star/black hole (1.4/10 $M_\odot$), black hole/black hole (10.7/10 $M_\odot$), and intermediate mass black hole binary (107/100$M_\odot$). Although our initial analyses looked at perfectly symmetric binaries, we ultimately chose slightly asymmetric binaries because there is a degeneracy in the Fisher Matrix associated with a symmetric binary, since the mass ratio is at a minimum. In some cases, we also look at an asymmetric massive black hole binary (150/50$M_\odot$). For all equations, we convert to units of seconds by setting $G = c = 1$. All computational work is done in Python. In order to achieve the numeric precision required for the Fisher Matrix analysis, those calculations are done using python's multiple precision floating point package, mpmath.

4.1 Sky-Averaged SNR

First, we computed the sky-averaged SNR for a100/100 $M_\odot$ black hole binary system. For a binary black hole system, we get[4]:

$$\mathrm{SNR}^2 = \frac{3}{20}\frac{2\mathcal{M}_L^{5/3}}{3\pi^{4/3}D_L^2}\int_0^\infty \frac{f^{7/3}}{S_n\left(f\right)}\,\mathrm{d}f \tag{7}$$

where D_L is luminosity distance ($D(1+z)$), $\mathcal{M}_L$ is the chirp mass ($\mathcal{M} = \frac{(m_1m_2)^{3/5}}{(m_1+m_2)^{1/5}}$) adjusted for redshift, f is the frequency of the gravitational wave, and $S_n(f)$ is the power spectral density (PSD) of the detector. The factor of $\frac{3}{20}$ accounts for averaging the detector sensitivity and binary orientation across the sky. We integrated over frequency starting at a year before merger (Equation 6), leading up to the frequency at the innermost stable circular orbit (Equation 1).

We see the results in Figure 3. On average, this shows that UNGO could detect a 100/100$M_\odot$ binary at a redshift of 1 (6.8 GPc) with roughly a SNR of 27. Moreover, the results show that on average, UNGO could see these binaries with significant SNR (> 5) out to about a redshift of 10, or 106 GPc, which is much farther than any of our current Earth-based detectors, which should be able to detect signals out to distances on the order of 100 MPc.

4.2 Angular Dependence of the SNR

Because the proposed UNGO geometry is similar to LISA, we were able to draw from [2] and [1] for the angular dependence.

We calculated the waveform as a function of the antenna pattern of the detector, given by [2]. The antenna pattern encodes the differences in detector sensitivity for different directions on the sky. The signal, h, is dependent on the antenna pattern of the detector:

$$\mathrm{h}_I(t) = F_{I+}(t)\mathrm{h}_+(t) + F_{I\times}(t)\mathrm{h}_\times(t). \tag{8}$$

The I subscript indicates that this gives the signal in a single detector.

To convert from the time-domain to the frequency domain,

$$\mathrm{t}(f) = t_0 - 5(8\pi f)^{-8/3}M_{total}^{-5/3}\left(1 + \left(\frac{4}{3}\right)\left(\frac{743}{336} + \frac{11}{4}\eta\right)x\right) \tag{9}$$

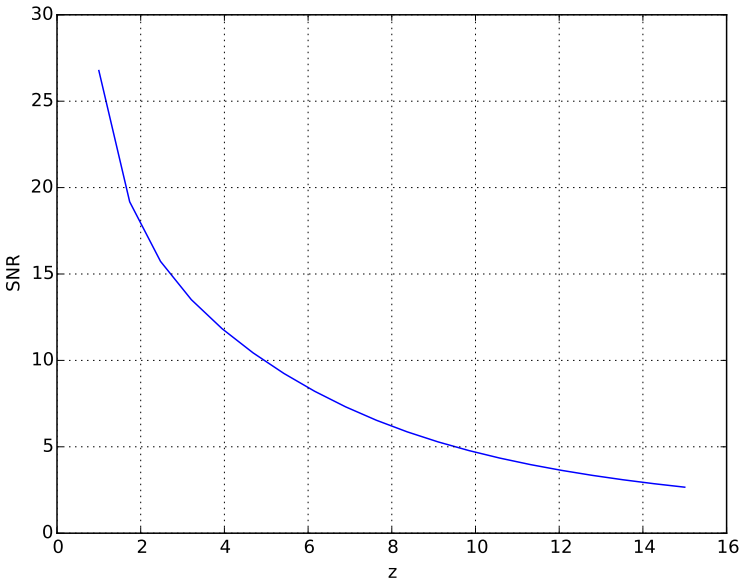

Figure 3: Sky-averaged SNR of a 100/100 $M_\odot$ binary black hole system as a function of redshift z. This plot shows that a 100/100 $M_\odot$ binary could be detected with a high SNR (> 25) out to roughly a redshift of 1, and with a significant SNR (> 5) out to roughly a redshift of 10 (around 100 GPc).

where η is the mass ratio of the binary $M_{total}\mu$, and x is the Post-Newtonian (PN) parameter $(\pi M_{total} f)^{2/3}$.

F_{I+} and $F_{I\times}$ are the antenna patterns of the 2-arm model,

$$F_{I+} = \frac{\sqrt{3}}{2} \times (\frac{1}{2}(1+\cos^2(\theta))\cos(2\phi)\cos(2\psi) - \cos(\theta)\sin(2\phi)\sin(2\psi)) \tag{10}$$

$$F_{I\times} = \frac{\sqrt{3}}{2} \times (\frac{1}{2}(1+\cos^2(\theta))\cos(2\phi)\sin(2\psi) + \cos(\theta)\sin(2\phi)\cos(2\psi)). \tag{11}$$

The angles θ, ϕ, and ψ are the latitude, longitude, and polarization angle of the source, in the detector's frame. The factor of $\sqrt{3}/2$ comes from the fact that the antennas are 60^o apart, not 90^o. For long duration sources, such as those we are trying to detect with UNGO, it is easier to work in a fixed, ecliptic-based coordinate system, rather than a detector-based coordinate system. To convert to to an ecliptic-based reference frame, we convert [1]:

$$\cos(\theta) = \frac{1}{2}\cos(\theta_S)\sqrt{\frac{3}{2}}\sin(\theta_S)\cos\left(\phi_0 + \frac{2\pi t}{T} - \phi_S\right) \tag{12}$$

$$\phi = \alpha_0 + \frac{2\pi t}{T} + \arctan\left(\frac{\sqrt{3}\cos(\theta_S) + \sin(\theta_S)\cos\left(\phi_0 + \frac{2\pi t}{T} - \phi_S\right)}{2\sin(\theta_S)\sin\left(\phi_0 + \frac{2\pi t}{T} - \phi_S\right)}\right) \tag{13}$$

$$\tan(\psi) = \Bigg[\frac{1}{2}\cos(\theta_L) - \frac{\sqrt{3}}{2}\sin(\theta_L)\cos\left(\phi_0 + \frac{2\pi t}{T} - \phi_S\right) - \cos(\theta)(\cos(\theta_L)\cos(\theta_S) + \sin(\theta_L)\sin(\theta_S)\cos(\phi_L - \phi_S))\Bigg] \Bigg/ \Bigg[\frac{1}{2}\sin(\theta_L)\sin(\theta_S)\sin(\phi_L - \phi_S) - \frac{\sqrt{3}}{2}\cos\left(\phi_0 + \frac{2\pi t}{T}\right)(\cos(\theta_L)\sin(\theta_S)\sin(\phi_S) - \cos(\theta_S)\sin(\theta_L)\sin(\phi_L)) - \frac{\sqrt{3}}{2}\sin\left(\phi_0 + \frac{2\pi t}{T}\right)(\cos(\theta_S)\sin(\theta_L)\cos(\phi_L) - \cos(\theta_L)\sin(\theta_S)\cos(\phi_S))\Bigg]. \quad (14)$$

Here, T is one year (in seconds), and (θ_S, ϕ_S) give the angular position of the source with respect to the solar ecliptic, and (θ_L, ϕ_L) correspond to the orientation of the source's angular momentum. ϕ_0 is the initial phase of the binary at the beginning of our detection, and α_0 corresponds to the initial orientation of the detector. For simplicity, we set both of these initial conditions to 0. We also assume here that the angular momenta of our sources' orbits are parallel to their spin.

For the signal, we consider the full waveform h in the frequency domain, including the first PN phase term. For a coalescing compact binary system [1],

$$\mathrm{h}(f) = \frac{Q}{D}\mathcal{M}^{5/6} f^{-7/6} \exp[i(\Psi(f) - \phi_P - \phi_D)] \quad (15)$$

where

$$Q = A_I \sqrt{\frac{5}{96}} \pi^{-2/3}. \quad (16)$$

A_I is the component of the prefactor that is dependent on the antenna pattern,

$$A_I = \sqrt{\alpha_+^2 F_{I+}(t)^2 + \alpha_\times^2 F_{I\times}(t)^2}, \quad (17)$$

where α_+ and $\alpha_\times$ are functions of the angle between the binary's spin and the line of sight [6]:

$$\alpha_+ = 1 + \cos^2(\theta_i) \quad (18)$$

$$\alpha_\times = -2\cos(\theta_i). \quad (19)$$

Here θ_i, the angle of inclination between the binary spin and the line of sight, is defined by

$$\cos(\theta_i) = \sin(\theta_S)\sin(\theta_L)\cos(\phi_L - \phi_S) + \cos(\theta_S)\cos(\theta_L). \quad (20)$$

$\Psi(f)$ is the phase of the signal [1]

$$\Psi(f) = 2\pi f t_c - \phi_c - \frac{\pi}{4} + \frac{3}{4}(8\pi\mathcal{M}f)^{-5/3}\left(1 + \frac{20}{9}\left(\frac{743}{336} + \frac{11}{4}\eta\right)(\pi\mathcal{M}_L f)^{\frac{2}{3}}\right) \quad (21)$$

where t_c and ϕ_c are the time and phase at coalescence, ϕ_P is the phase associated with the detector's motion

$$\tan(\phi_P) = \frac{-\alpha_\times F_{I\times}}{\alpha_+ F_{I+}}, \quad (22)$$

and ϕ_D is the Doppler phase term

$$\phi_D = 2\pi f \left(\frac{1\ AU}{c}\right) \sin(\theta_S)\cos(\phi_0 + 2\pi t/T - \phi_S)(\text{where} T = 1\text{yr}). \tag{23}$$

The complex phase terms cancel out when calculating the SNR, but will be useful later when looking at the Fisher Matrix and parameter estimation errors.

Because the UNGO design has 3 satellites, we could also envision a 3-arm antenna pattern, which would be more in line with the dual-detector model of LISA. This 3-arm pattern would function as the equivalent of 2 detectors. Therefore, we wrote code for the antenna pattern of a second detector, although for our initial calculations, we chose conservatively to assume UNGO will have only one detector. For the second detector, the formulas are the same, with the exception that the antenna pattern is instead [1]:

$$F_{II+} = \frac{\sqrt{3}}{2} \times (\frac{1}{2}(1+\cos^2(\theta))\sin(2\phi)\cos(2\psi) + \cos(\theta)\cos(2\phi)\sin(2\psi)), \text{ and} \tag{24}$$

$$F_{II\times} = \frac{\sqrt{3}}{2} \times (\frac{1}{2}(1+\cos^2(\theta))\sin(2\phi)\sin(2\psi) - \cos(\theta)\cos(2\phi)\cos(2\psi)). \tag{25}$$

which is equivalent to the first antenna pattern, with $\theta_{\rm II} = \theta$, $\psi_{\rm II} = \psi$, and $\phi_{\rm II} = \phi - \frac{\pi}{4}$ [2]. Note that we have chosen to include the factor of $\frac{\sqrt{3}}{2}$ inside the antenna pattern, whereas [2] and [1] include it elsewhere.

4.3 Verifying the Accuracy of the Angular-dependent SNR

In order to verify the accuracy of our angular-dependent SNR calculations, we evaluated the SNR^2 at 1000 random sky positions, and took the average value. We repeated this for 7 different redshifts, $z = 1$ - $z = 7$, and plotted the results against our sky-averaged SNR function (Equation 7). See Figure 4.

5 SNR Results

Given our confidence in our antenna pattern, we calculated the SNR for a 100/100 $M_\odot$ binary black hole system as a function of redshift for several different sky positions. Figure 5 shows the SNR as a function of redshift for different angular positions with respect to the solar ecliptic for a 100/100 $M_\odot$ binary black hole system.

We then compared the performance of the detector for a 2-arm and a 3-arm antenna pattern. As we see in Figure 6, the 2-arm model can detect a binaries out to cosmological distances, and the 3-arm model performs even better by roughly a factor of 2. We defined the farthest detectable binary as being at a given position and orientation (in this case, $\theta_S = \phi_S = \theta_L = \phi_L = 0$) with a SNR > 8, to be consistent with other literature. A peak occurs around masses of 10 $M_\odot$, after which point the signal moves out of the UNGO frequency band, as more massive binaries coalesce at lower and lower frequencies. To give a better sense of

Figure 4: SNR of a 100/100 $M_\odot$ binary black hole system as a function of redshift z, averaged over random sky positions. The wider green error bars correspond to the standard deviation, and the tiny red error bars correspond to standard error of the mean. The lower plots indicate that the locations and orientations were evenly and randomly distributed. This consistency thus validates both the angle-averaged and angular dependent SNR code.

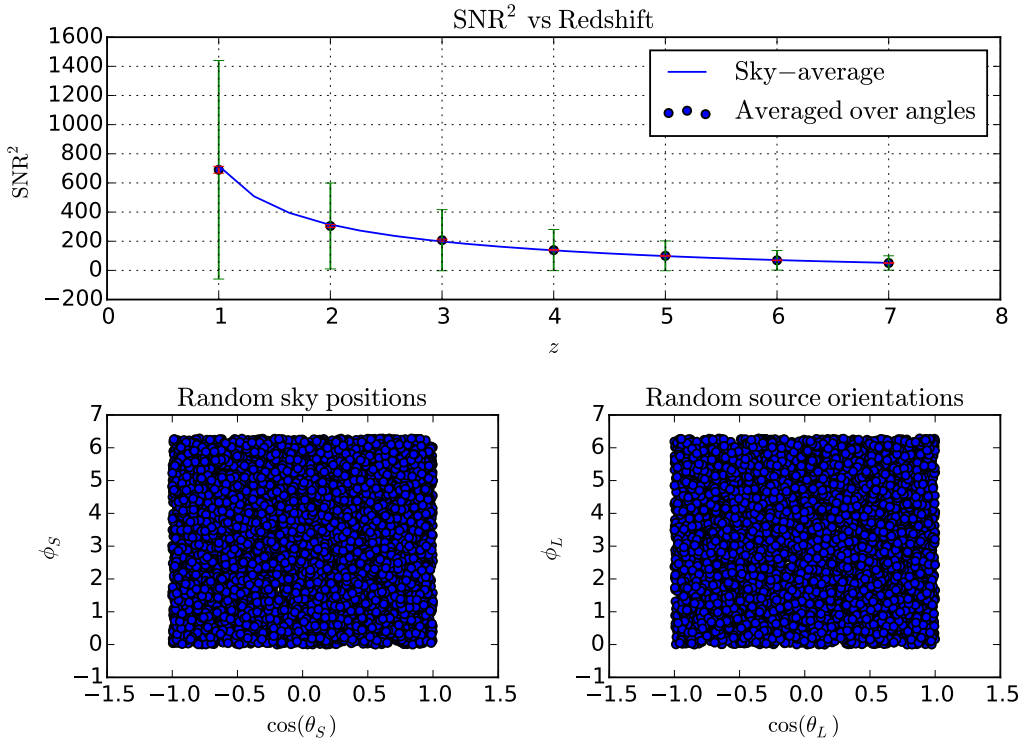

this detector's abilities compared to other proposed missions, Figure 7 is taken directly from [11], and describes the range to which the proposed Einstein Telescope could detect signals if operating at design sensitivity. Although the two do not look at exactly the same system, it is clear that the UNGO mission performs better for higher mass binaries, and UNGO is otherwise generally on par with the speculative ground-based Einstein Telescope.

6 Fisher Matrix Analysis Results

After calculating the SNR and discerning to what extent the detector is capable of hearing signals, we calculated the detector's ability to extract information from those signals. We attempted to find the Fisher Matrix for 9 parameters: relative redshift-adjusted chirp mass $\ln(\mathcal{M}_L)$, mass ratio η, relative luminosity distance $\ln(D_L)$, sky position (θ_S, ϕ_S), binary orientation (θ_L, ϕ_L), time of coalescence t_c, and phase at coalescence ϕ_c. This proved to be difficult for a number of reasons. Foremost, for the 2-arm antenna pattern, the luminosity Distance parameter (D_L) turned out to be highly degenerate with the binary orientation

Figure 5: SNR vs redshift for 100/100 $M_\odot$ head-on binary: (left to right, top to bottom) $\theta_S = \theta_L = 0$, $\pi/12$, $\pi/6$, $\pi/4$, $\pi/3$, $5\pi/12$, $\pi/2$; $\phi_S = \phi_L = 0$

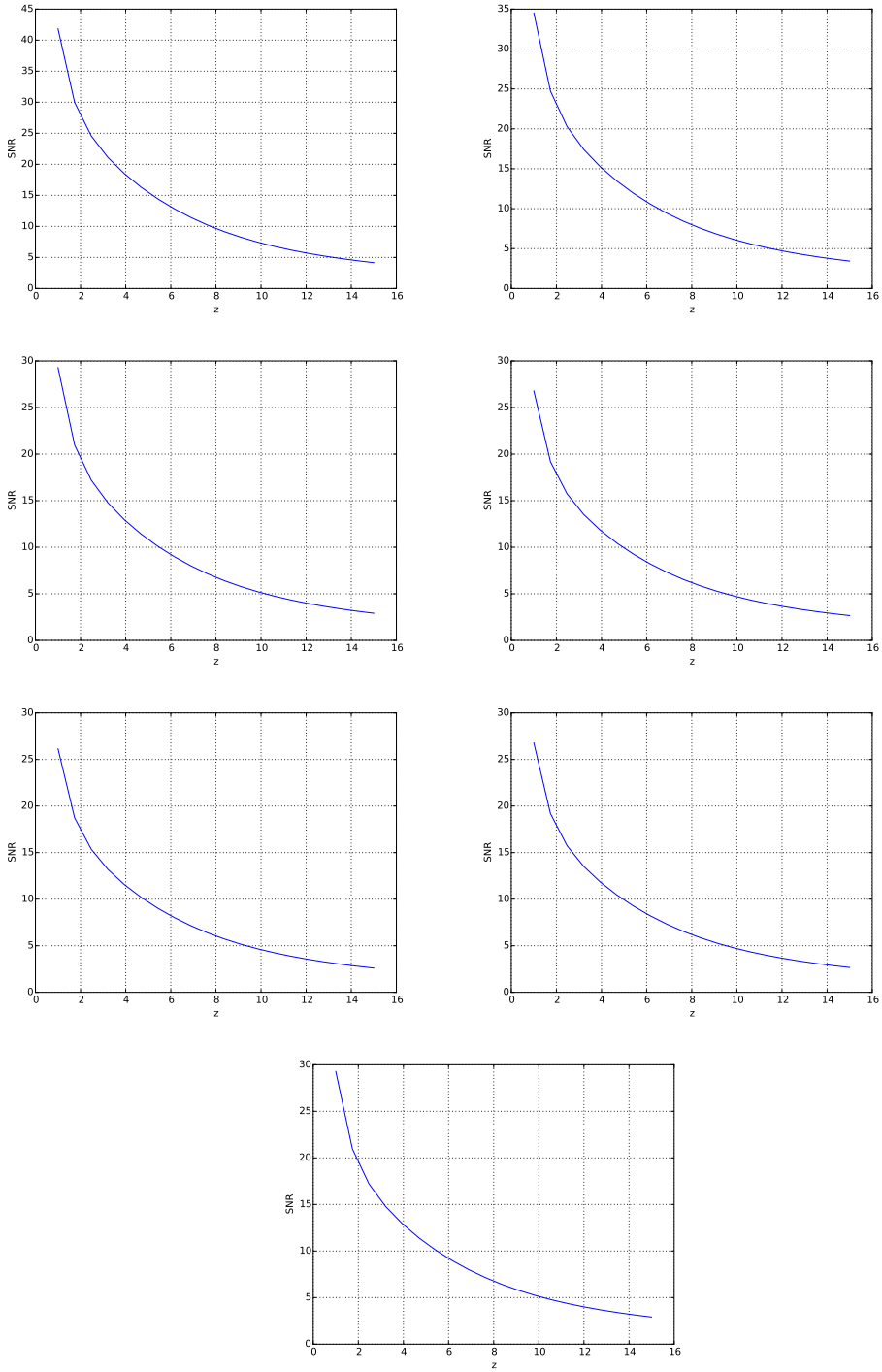

Figure 6: Farthest detectible symmetric binary as a function of mass. Detectibility is determined by SNR>8, as in the Einstein Telescope literature [11]. For this example, we look at head-on overhead binaries: $\theta_S = \phi_S = \theta_L = \phi_L = 0$.

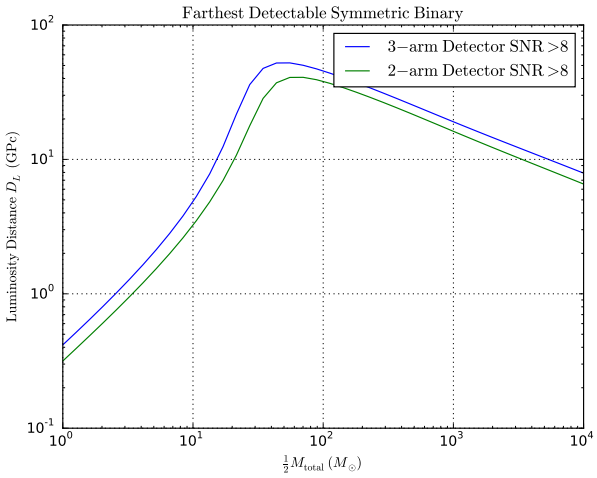

Figure 7: Figure from Sathyaprakash et al. detailing the Einstein Telescope's reach [11]. Although the sources are slightly different, as this figure considers asymmetric binaries while we consider symmetric binaries, it shows that UNGO has a similar ability to detect sources of smaller masses, and a greater ability to detect sources of greater masses.

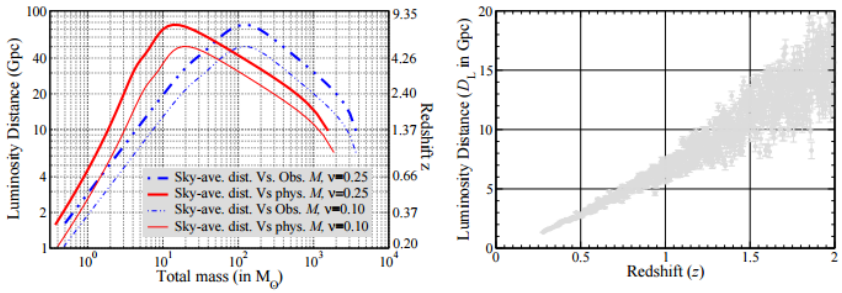

FIG. 1: The left panel shows the range of the Einstein Telescope for inspiral signals from binaries as a function of the *intrinsic* (red solid line) and *observed* (blue dashed line) total mass. We assume that a source is visible if it produces an SNR of at least 8 in ET. The right panel shows a realization of the source catalogue showing the *measured* luminosity distance (inferred from GW observation of neutron star-black hole mergers) versus their red-shift (obtained by optical identification of the source). This catalogue is then fitted to a cosmological model.

angles (θ_L and ϕ_L). This is because all of these parameters solely affect the amplitude of the waveform, rather than its phase evolution. Changing the parameter space helped a little bit. By modifying our parameter space to include $\ln(\mathcal{M})$ instead of $\ln(\mathcal{M}_L)$, and getting $\mathcal{M}_L$ from the redshift extracted from D_L, we were able to break some, but not all, of the degeneracy there. Plotting the integrands of the inner products in each Fisher Matrix element for a 150/50 $M_\odot$ binary system, as well as the integrands without the PSD ($S_h(f)$) of the detector, sheds light on the issue. As we can see in Figure 13, for most parameters,

the majority of the signal variation comes from the lower-frequency domain, but that is also where the majority of the noise lies. This is why many of the integrand plots have nearly the same form, to some constant factor, as the integrand of the SNR^2 inner product $(h|h)$ (See Figure 14), resulting in high degeneracies.

This was further confirmed by shifting the PSD to the left 2 orders of magnitude (by integrating over $S_n(100f)$). When we did so, the 3-parameter inverse Fisher Matrix of the most degenerate parameters, $\ln(D_L)$, θ_L, and ϕ_L gave much more reasonable estimates for the variances (on the order of 10^{-2} radians, as opposed to 10^2 radians). This allowed for much more successful determination of these three parameters individually. See Table 1.

	Standard $S_n(f)$	Shifted $S_n(100f)$
Parameter	δ(Parameter)	δ(Parameter)
$\ln(D_L)$	214.5	0.05859
θ_L	338.7	0.08800
ϕ_L	71.74	0.01968

Table 1: Single-parameter errors for the most degenerate parameters, for the current UNGO noise curve, and the noise curve shifted left by 2 orders of magnitude.

Therefore, we discovered that, given the current noise curve, localization of a GW signal from a 100/100 $M_\odot$ binary at $z = 2$ (16 GPc) is not possible. For an intermediate-mass black hole binary, the gravitational wave signal only reaches the most sensitive region of the noise curve at 70s prior to merger, while the detector's motion is on a timescale of a year, making one rotation about the sun, and one rotation about its axis. This is not enough time for the detector's changing orientation to vary the signal enough to locate a source. Although UNGO cannot locate sources nearly as far as it can detect them, it still should be able to extract parameters under less extreme conditions. Therefore, we focused our efforts on discerning what kind of sources could be localizable.

Although the parameter estimation errors were large for binaries at high redshifts (>1), at more modest distances and for less massive binaries, the Fisher Matrix calculation was substantially more stable. We then calculated the Fisher Matrix for different binaries, comparing a 2-arm and a 3-arm antenna pattern. In order to avoid any inherent degeneracies, we used a semi-random set of base parameters that yield a similar SNR to the sky-averaged SNR: $\theta_S = 0.7$ rad, $\phi_S = 4.1$ rad, $\theta_L = 1.3$ rad, $\phi_L = 3.1$ rad, $t_c = 12.0$ s, and $\phi_c = 1.0$ rad.

For certain parameters, the 3-arm detector model performs substantially better than the 2-arm model, which makes the overall Fisher Matrix more reliable as well. Tables 2 and 3 show the diagonal elements of the inverse Fisher Matrix for 2 different binary systems. Although some parameters are much more well-constrained than others, the most interesting parameters, including mass, distance, and sky location, seem to be fairly well-constrained for both the 2-arm and 3-arm antennae. Other parameters, such as the binary's orientation, and the phase at chirp, are substantially better constrained with a 3-arm detector.

Additionally, incorporating the covariance errors in sky position acquired from the inverse Fisher Matrix, we can calculate the solid-angle error $\Delta\Omega = \sin(\theta_S)\sqrt{\delta^2\theta_S}\sqrt{\delta^2\phi_S} - \delta\phi_S\theta_S$.

D_L	Arms	$\delta \ln(\mathcal{M})$	$\delta\eta$	$\delta \ln(D_L)$	$\delta\theta_S$	$\delta\phi_S$	$\delta\theta_L$	$\delta\phi_L$	δt_c (s)	$\delta\phi_c$
50 MPc	2	3.8e-6	4.1e-5	3.3e-4	1.5e-3	1.1e-3	0.37	0.33	0.51	1.36
50 MPc	3	3.0e-6	2.9e-5	2.5e-4	1.1e-3	6.8e-4	2.8e-2	3.4e-3	0.35	0.11
10 GPc	2	8.4e-6	4.8e-3	2.3e-5	0.12	0.24	43.9	38.5	82.9	158.
10 GPc	3	6.1e-6	3.4e-3	1.6e-5	8.0e-2	0.15	1.65	2.00	51.0	6.46

Table 2: Single-parameter errors of a 1.5/1.4 $M_\odot$ binary, for the current UNGO noise curve, comparing a 2-arm detector and a 3-arm detector.

D_L	Arms	$\delta \ln(\mathcal{M})$	$\delta\eta$	$\delta \ln(D_L)$	$\delta\theta_S$	$\delta\phi_S$	$\delta\theta_L$	$\delta\phi_L$	δt_c (s)	$\delta\phi_c$
50 MPc	2	7.0e-3	2.9e-5	0.57	1.5e-2	1.3e-2	0.45	0.45	4.93	1.51
50 MPc	3	3.0e-5	2.0e-5	2.4e-4	5.8e-3	7.9e-3	9.3e-3	4.8e-3	3.09	3.1e-3
10 GPc	2	2.5e-3	4.4e-3	4.8e-3	3.82	2.66	50.2	42.1	1065	178
10 GPc	3	7.5e-4	3.1e-3	1.5e-3	1.75	1.35	2.59	0.26	735	0.63

Table 3: Single-parameter errors of a 100/107 $M_\odot$ binary, for the current UNGO noise curve, comparing a 2-arm detector and a 3-arm detector.

Figures 8, 10 and 11 show the error in solid angle as a function of distance for 4 different binary systems: 1.5/1.4 $M_\odot$ neutron star (NS)/NS, 1.4/10.0 NS/black hole (BH), 10.0/10.0 $M_\odot$ BH/BH, and 100.0/100.0 $M_\odot$ BH/BH. Dashed lines are added to show the maximum distances that the binary system could be localized to within a solid angle of 10^{-4} steradians.

With this information, we then calculated the farthest binary that the detector could locate within a (slightly looser) threshold of 10^{-3} steradians (at our arbitrary location and orientation) as a function of binary mass, shown in Figure 12. These distances are substantially smaller than the detector's range of hearing signals (recall Figure 6), but they still allow localization out to ~ 1 GPc. For the most part, the detector is well-equipped to localize many aLIGO sources, and so synthesizing the data streams of the two detectors could be very useful for cosmography.

7 Other Noteworthy Challenges

Because there is so much literature on the subject, and each article employs slightly different conventions, it was a challenge to find an accurate, standard way to model our signal and compute the SNR and Fisher Matrix. Moreover, because we are writing code for a complicated set of equations, we have also encountered many cases where our code is working properly but we have to be very careful about how to interpret it. Additionally, getting to the bottom of the source of the degeneracy in the Fisher Matrix was very difficult. We had to convince ourselves that the degeneracies in the Fisher Matrix were not a problem in our code, but rather a fundamental problem with the detector. Other challenges included the fact that many of the Fisher Matrix derivatives needed to be taken numerically, which often proved to be fairly unstable. Additionally, the Fisher Matrix was typically nearly degener-

Figure 8: $\Delta\Omega$ for a 1.5/1.4 $M_\odot$ binary. Anything to the left of the dashed lines can be localized within a solid angle of 10^{-4} steradians.

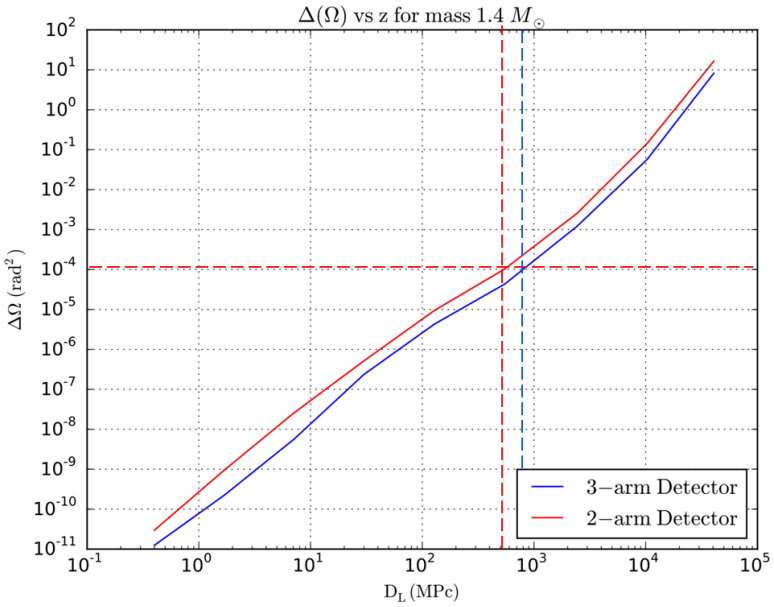

Figure 9: $\Delta\Omega$ for an asymmetric 1.4/10.0 $M_\odot$ binary. Anything to the left of the dashed lines can be localized within a solid angle of 10^{-4} steradians.

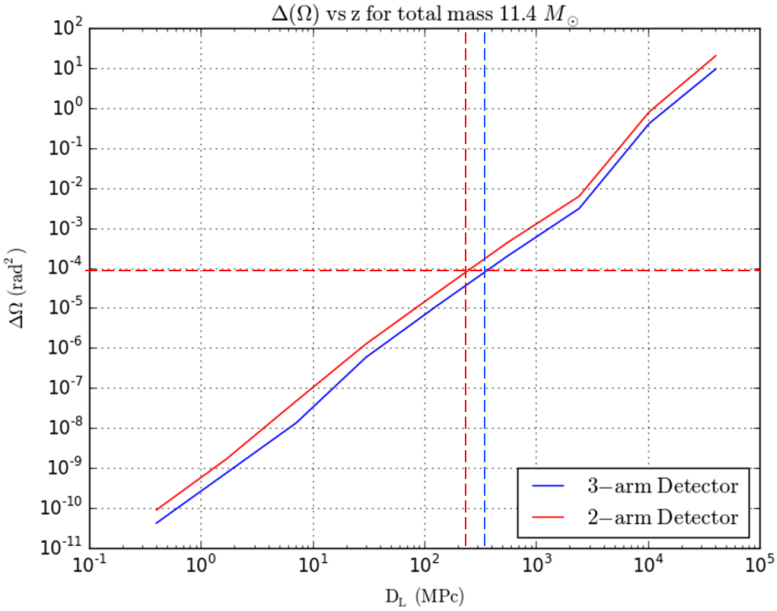

Figure 10: $\Delta\Omega$ for a 10.7/10 $M_\odot$ binary. Anything to the left of the dashed lines can be localized within a solid angle of 10^{-4} steradians.

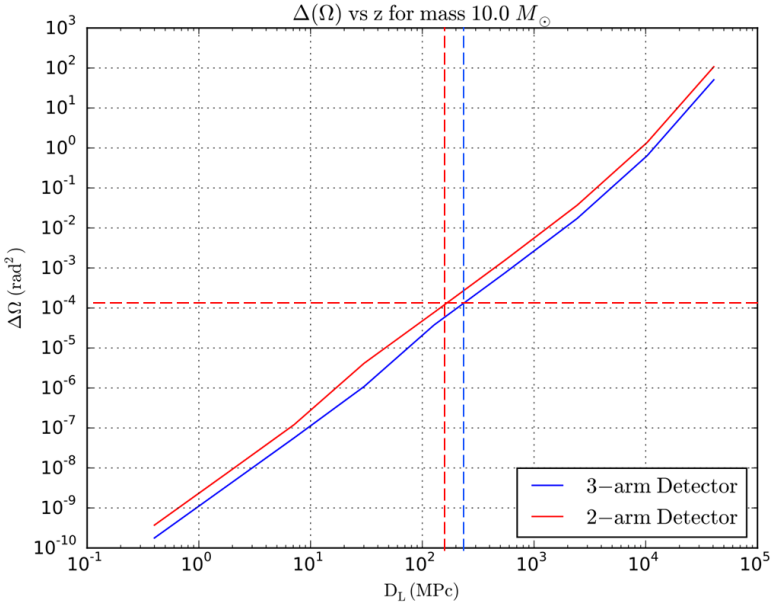

Figure 11: $\Delta\Omega$ for a 107/100 $M_\odot$ binary. Anything to the left of the dashed lines can be localized within a solid angle of 10^{-4} steradians.

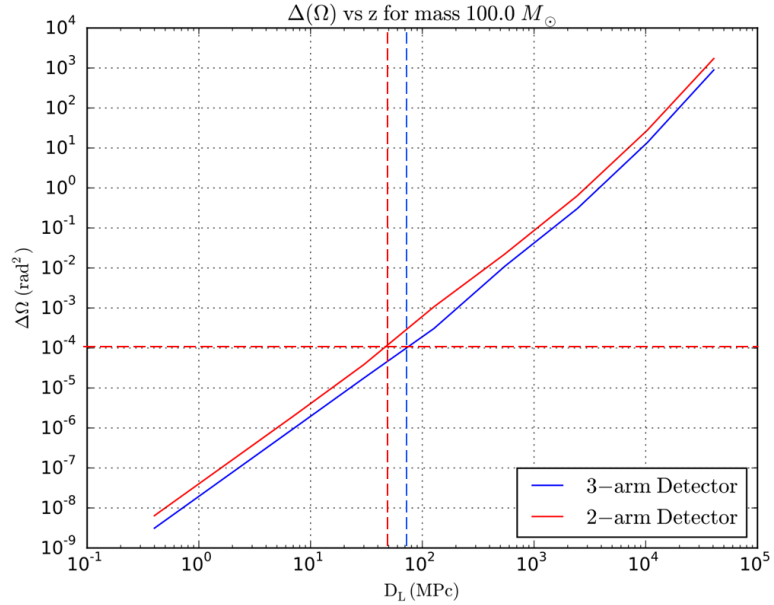

Figure 12: Farthest localizable nearly symmetric binary ($M_1 = \frac{1.5}{1.4} M_2$) as a function of mass. Localizability is defined here by $\Delta\Omega < 0.001$. Binary characteristics are $\theta_S = 0.7$ rad, $\phi_S = 4.1$ rad, $\theta_L = 1.3$ rad, $\phi_L = 3.1$ rad, $t_c = 12.0$ s, and $\phi_c = 1.0$ rad.

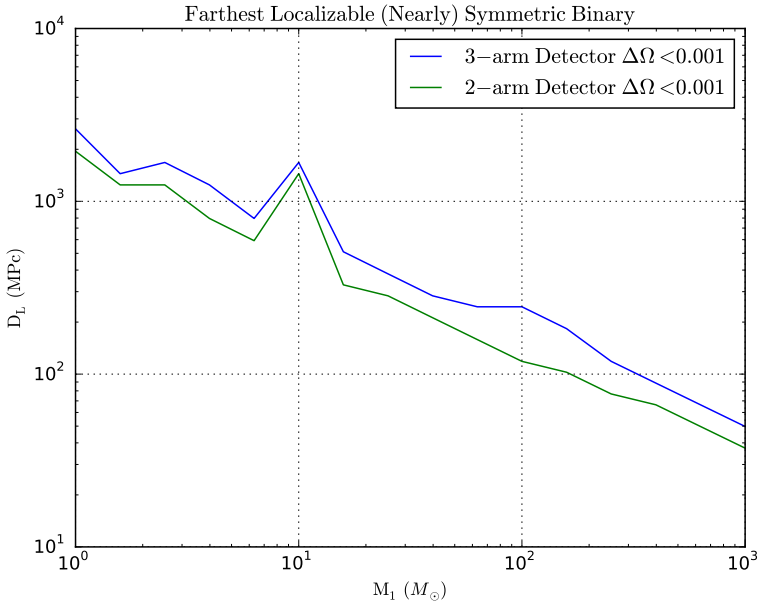

ate, so inverting it in a reliable way was tricky. Perhaps the largest problem with the Fisher Matrix analysis was the fact that machine numeric roundoff error could often dominate our results. Recall that in Figure 13, we see that the Fisher Matrix calculations are dominated by the (constant) noise curve far more than by the actual variations in the signal. In order to account for this problem, we implemented arbitrary precision using a python package called mpmath. Using 20 decimal places of precision and the more precise built-in mpmath integration techniques, we were able to more accurately calculate and invert the Fisher Matrix for all binaries. We compared the improved python Fisher Matrix code against a Wolfram Mathemateca implementation of the code (which also employed arbitrary precision), and the two were consistent.

8 Conclusions

For a space-based gravitational-wave detector, UNGO has a number of advantages. Foremost, it is substantially less costly than other proposed missions (our current estimates put it at under 1 billion dollars). Moreover, given its range of sensitivity, its data stream could be synthesized with LIGO's for better detection, and most likely better parameter estimation. As we have seen, UNGO can detect binary systems out to cosmological distances, and it has the ability to localize even massive sources up to ~ 1 GPc away. Thus, it would be useful in giving an early warning for aLIGO sources (such as binary neutron stars at luminosity distances of 50-100 MPc). However, at some masses and redshifts, particularly distant redshifts

and higher masses, the detector struggles to estimate certain important parameters such as the binary's orientation and the time and phase of coalescence. Additionally, with its higher noise curve, the UNGO mission is not as robust as other space based missions. However, in order to fully assess UNGO's capability to detect gravitational waves from a wider variety of sources, more work is required.

9 Future Work

Given the functionality of our Fisher Matrix code, we could easily go on to make heat maps of the error in the various parameters as a function of location in the sky for the various binary systems. This will allow us to better assess how long an object can stay within the same section of UNGOs detection field, and will allow us see how accurately we could point other electromagnetic telescopes at the sources. However, given time constraints, and the large amounts of time that it takes for the Fisher Matrix code to run, those maps could not be included in this paper. Thus, they are left as future work, as is making the Fisher Matrix code run faster, perhaps by delegating pieces of the code to multiple cores (especially codes such as the sky-map code, which require many Fisher Matrix calculations). Future work also is needed to analyze the improvement to this detector's sensitivity if its data stream is synthesized with the data from aLIGO. This will be done by simply converting sky-location parameters from aLIGO's earth-based coordinate system to the ecliptic-based coordinate system that our analysis considers, calculating the Fisher Matrix for the aLIGO noise curve using those parameters, adding that matrix to the UNGO Fisher Matrix for the same source, and inverting. In addition, future work should consider sources other than coalescing compact binaries, different mass-ratios, et cetera.

10 Acknowledgements

A tremendous thank you goes to Tom Callister, for your constant help and support, and for always having a positive outlook. Thank you also to Dr. Rana Adhikari for your experience, perspective, help and advice, and for the brilliant UNGO concept. Thank you to Dr. Curt Cutler for your help and expertise in all things related to space-based GW detectors. Thank you to Elvira Kinzina for our helpful discussions and your collaboration and insight, and for introducing us to mpmath, which was immensely helpful. Thank you to Dr. Tjonnie Li for your knowledge and experience with the difficulties of Fisher Matrices, and for helping every SURF student who needed it. I would also like to thank all of my fellow LIGO SURFs for helpful discussions, support, and more. And of course, thank you to the LIGO Scientific Collaboration, the Caltech SURF program and the NSF for the funding and for making this program possible.

Figure 13: Checking the Partial Derivatives in the Fisher Matrix elements. Integrands of the inner product of the listed derivatives, as well as just the numerators (everything without the detector PSD), are plotted vs GW frequency. These derivatives are for a 150/50 $M_\odot$ binary, at the arbitrary position and orientation. Together, these plots show the strong degeneracy between certain parameters.

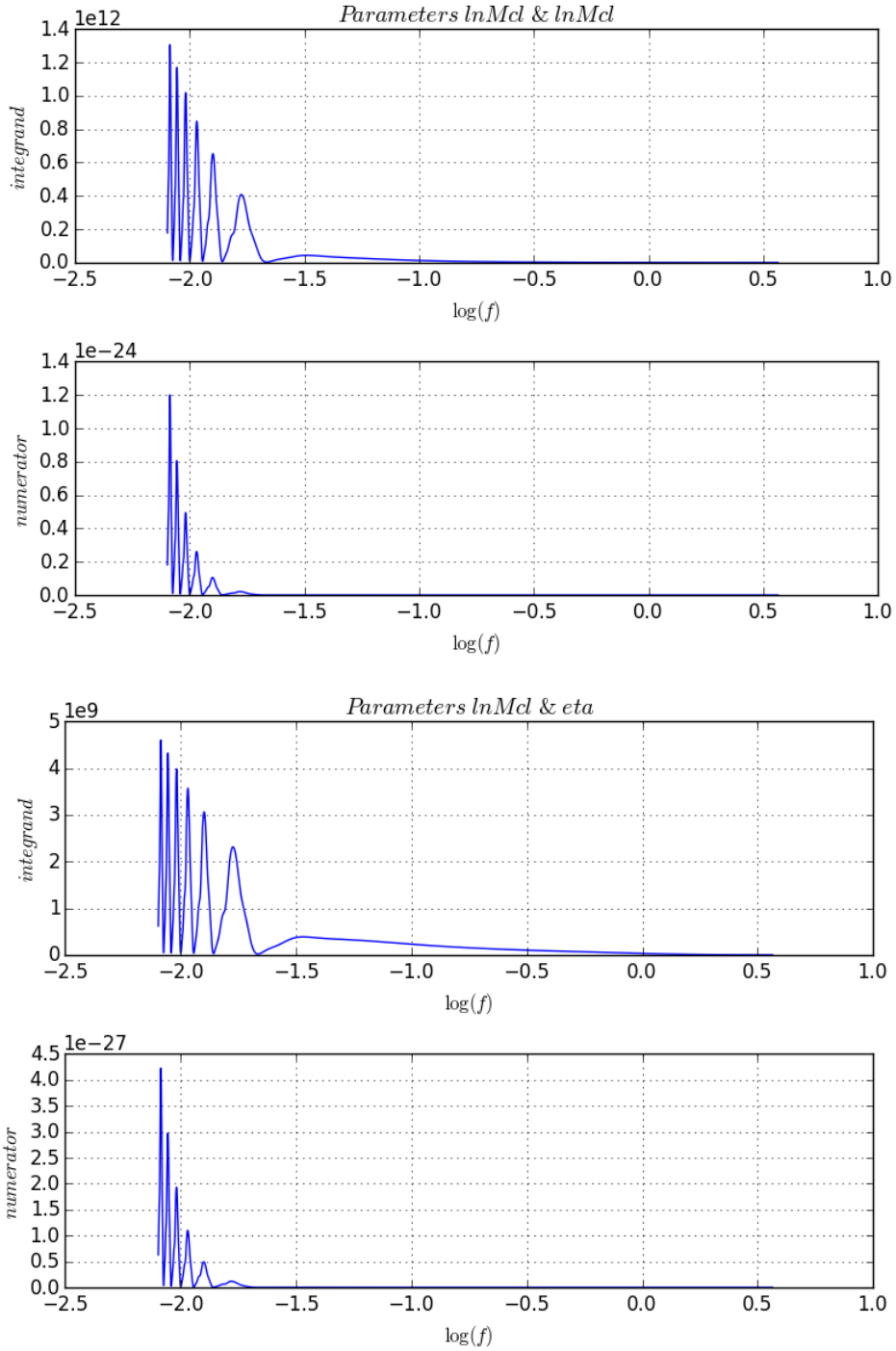

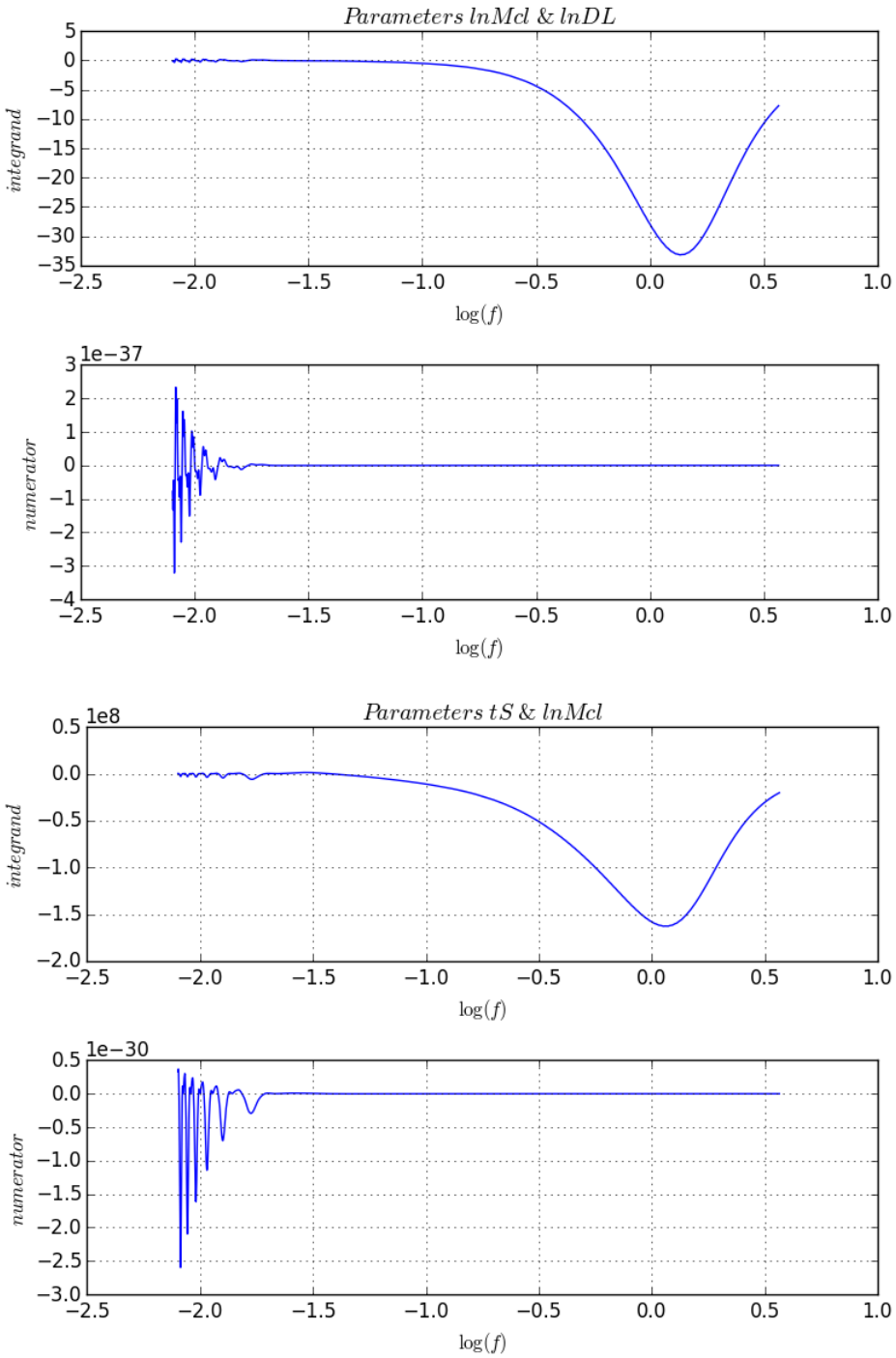
Parameters lnMcl & lnDL
integrand
log(f)
1e−37
numerator
log(f)
Parameters tS & lnMcl
1e8
integrand
log(f)
1e−30
numerator
log(f)

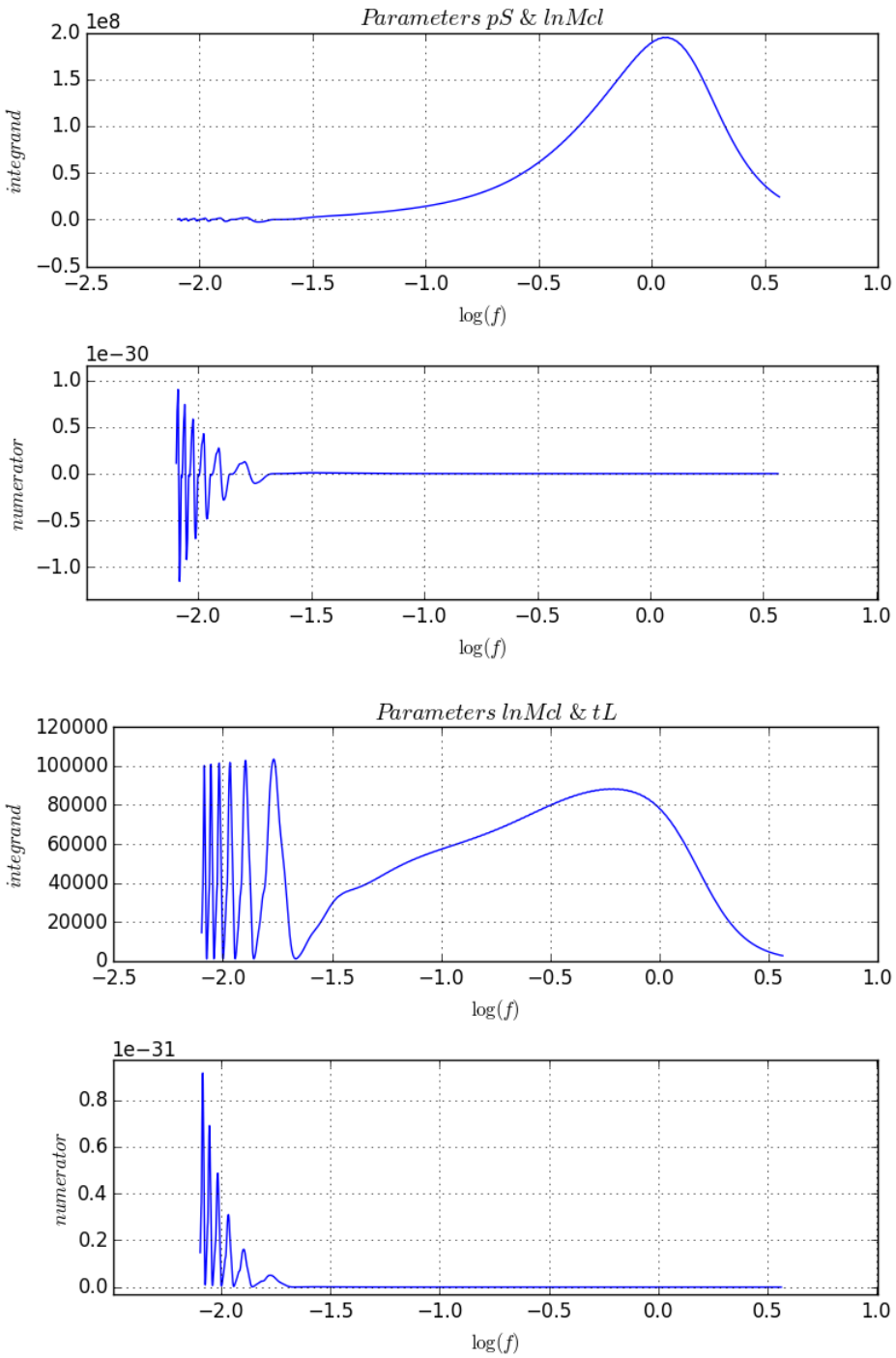
Parameters pS & lnMcl
1e8
integrand
log(f)
1e−30
numerator
log(f)
Parameters lnMcl & tL
integrand
log(f)
1e−31
numerator
log(f)

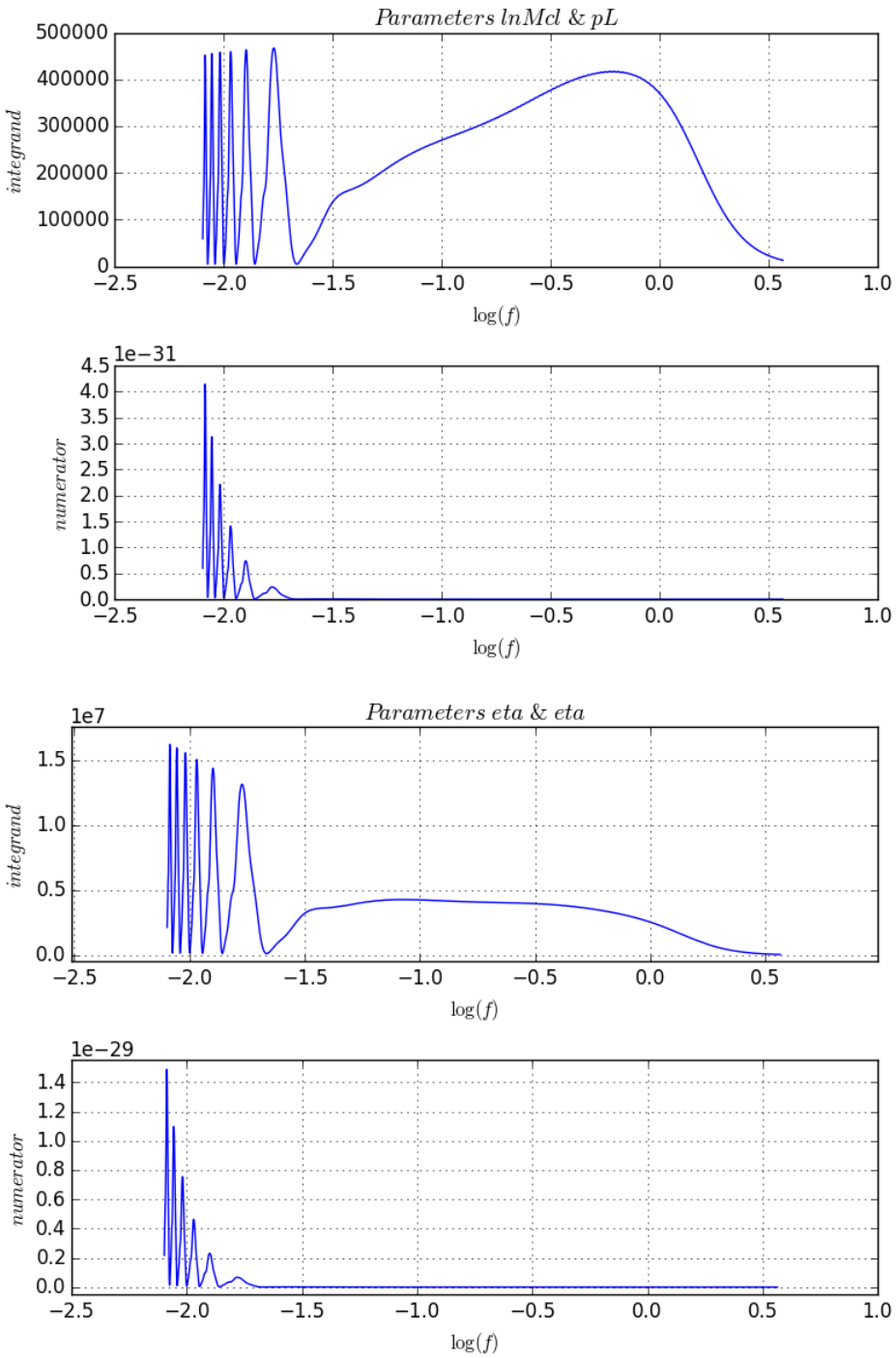
Parameters lnMcl & pL
integrand
log(f)
1e−31
numerator
log(f)
Parameters eta & eta
1e7
integrand
log(f)
1e−29
numerator
log(f)

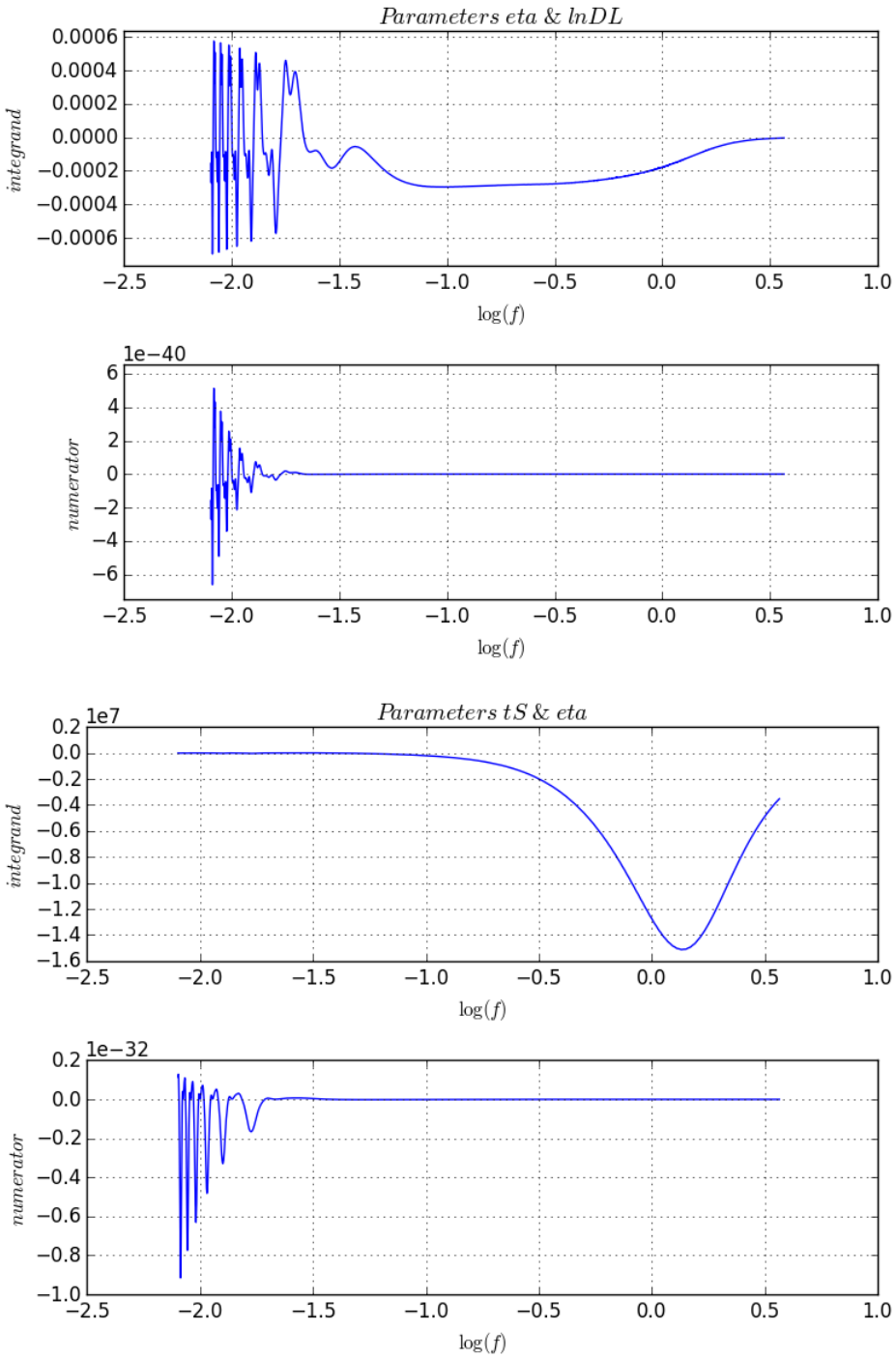
Parameters eta & lnDL
integrand
log(f)
1e−40
numerator
log(f)
Parameters tS & eta
1e7
integrand
log(f)
1e−32
numerator
log(f)

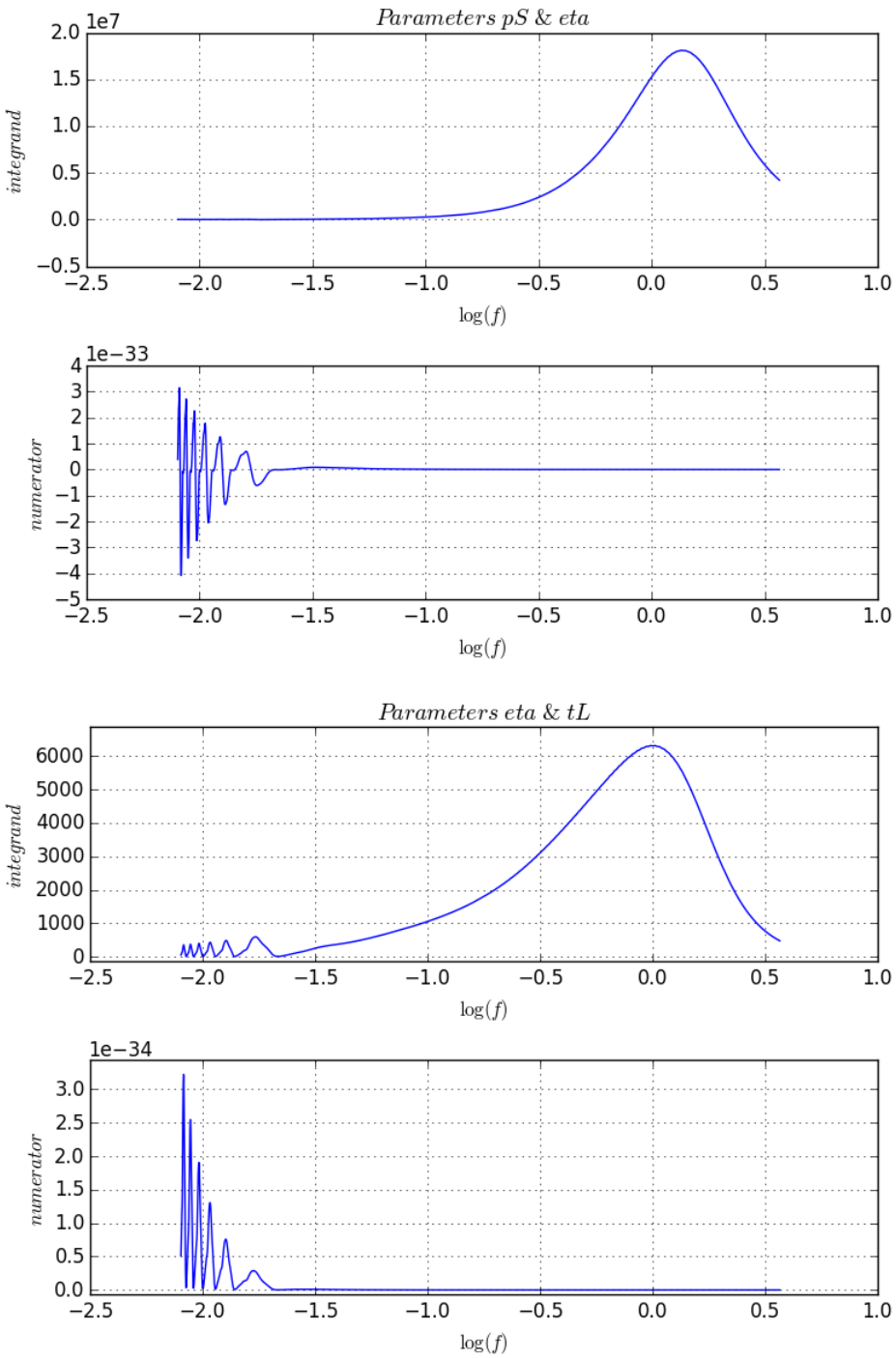
Parameters pS & eta
1e7
integrand
log(f)
1e−33
numerator
log(f)
Parameters eta & tL
integrand
log(f)
1e−34
numerator
log(f)

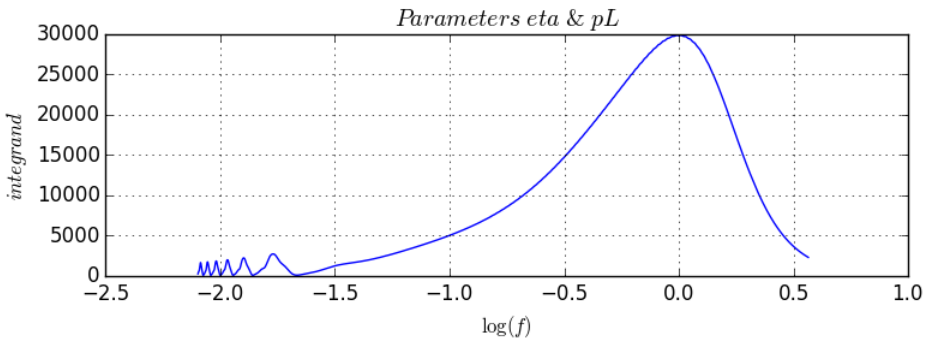
Parameters eta & pL
integrand
log(f)

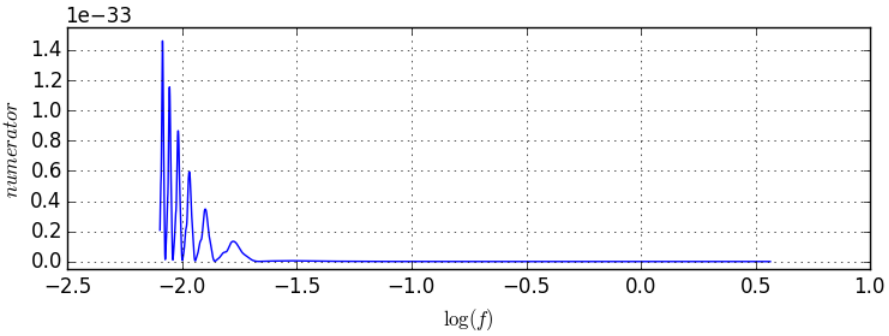
1e−33
numerator
log(f)

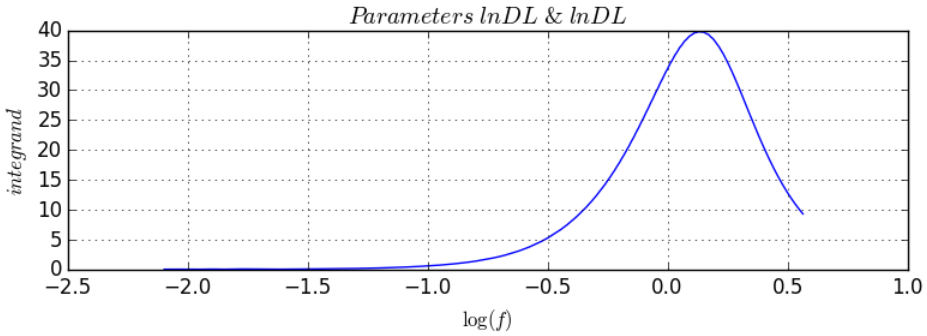
Parameters lnDL & lnDL
integrand
log(f)

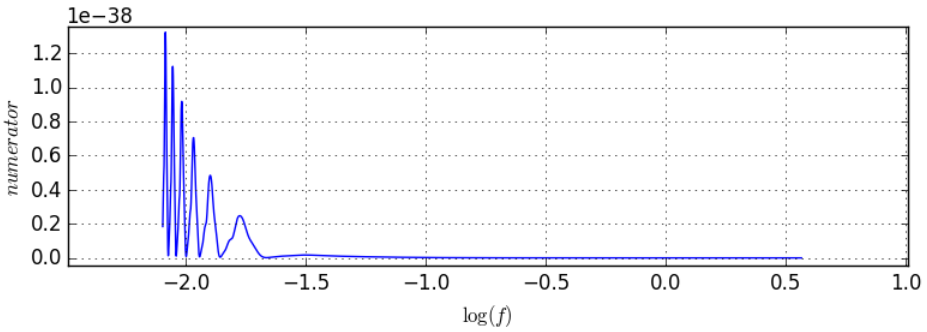
1e−38
numerator
log(f)

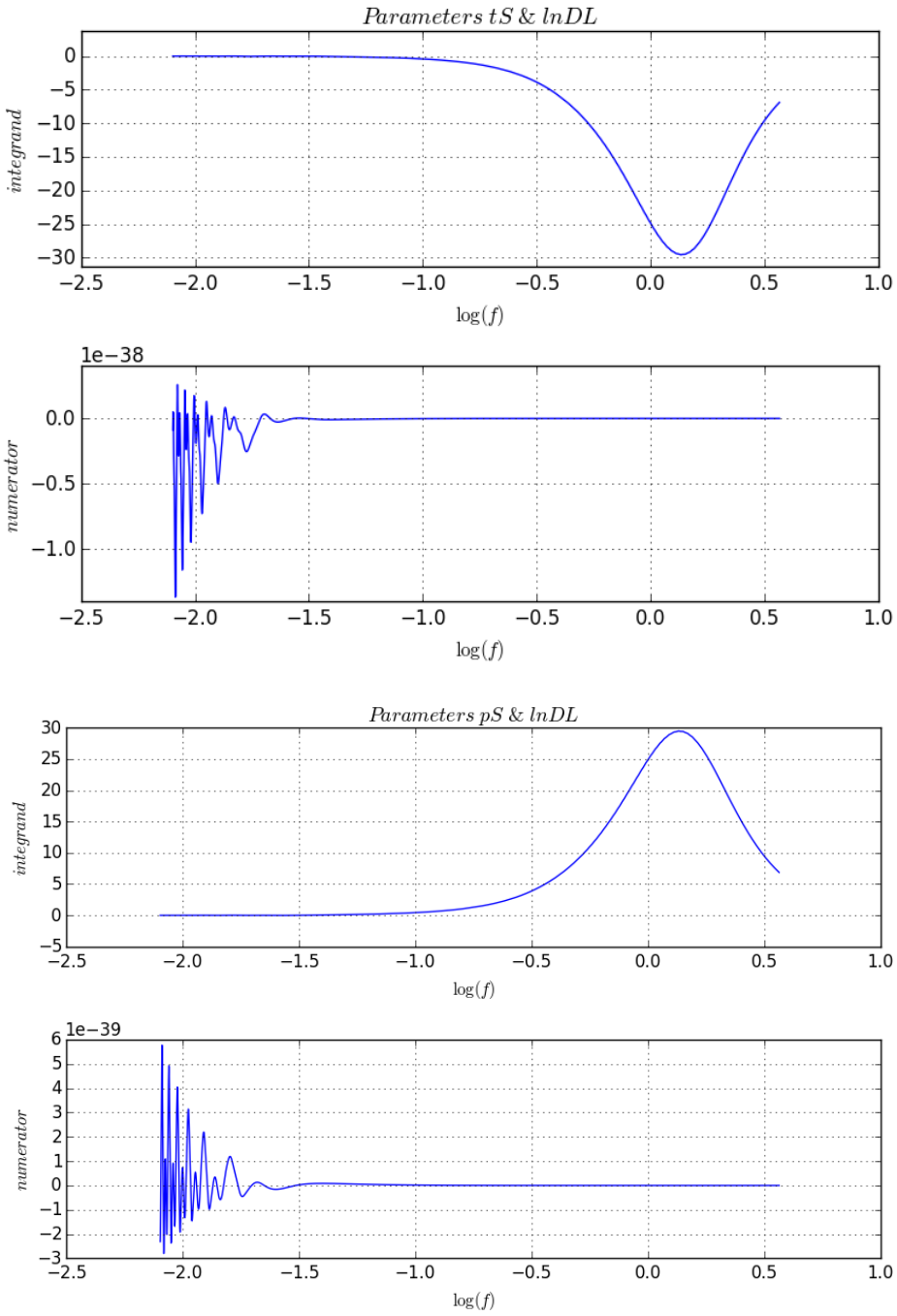
Parameters tS & lnDL
integrand
log(f)
1e−38
numerator
log(f)
Parameters pS & lnDL
integrand
log(f)
1e−39
numerator
log(f)

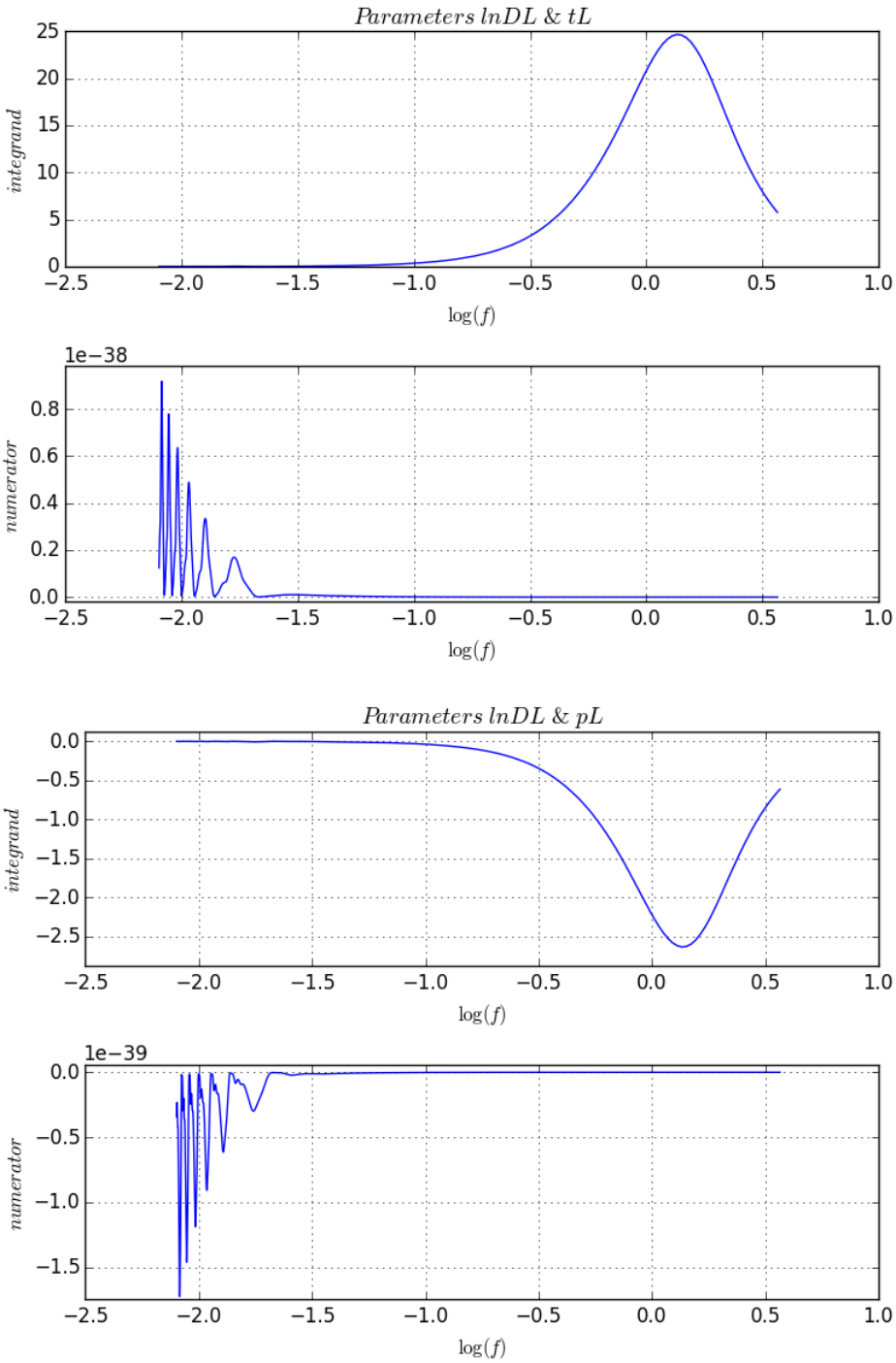
Parameters lnDL & tL
integrand
log(f)
1e−38
numerator
log(f)
Parameters lnDL & pL
integrand
log(f)
1e−39
numerator
log(f)

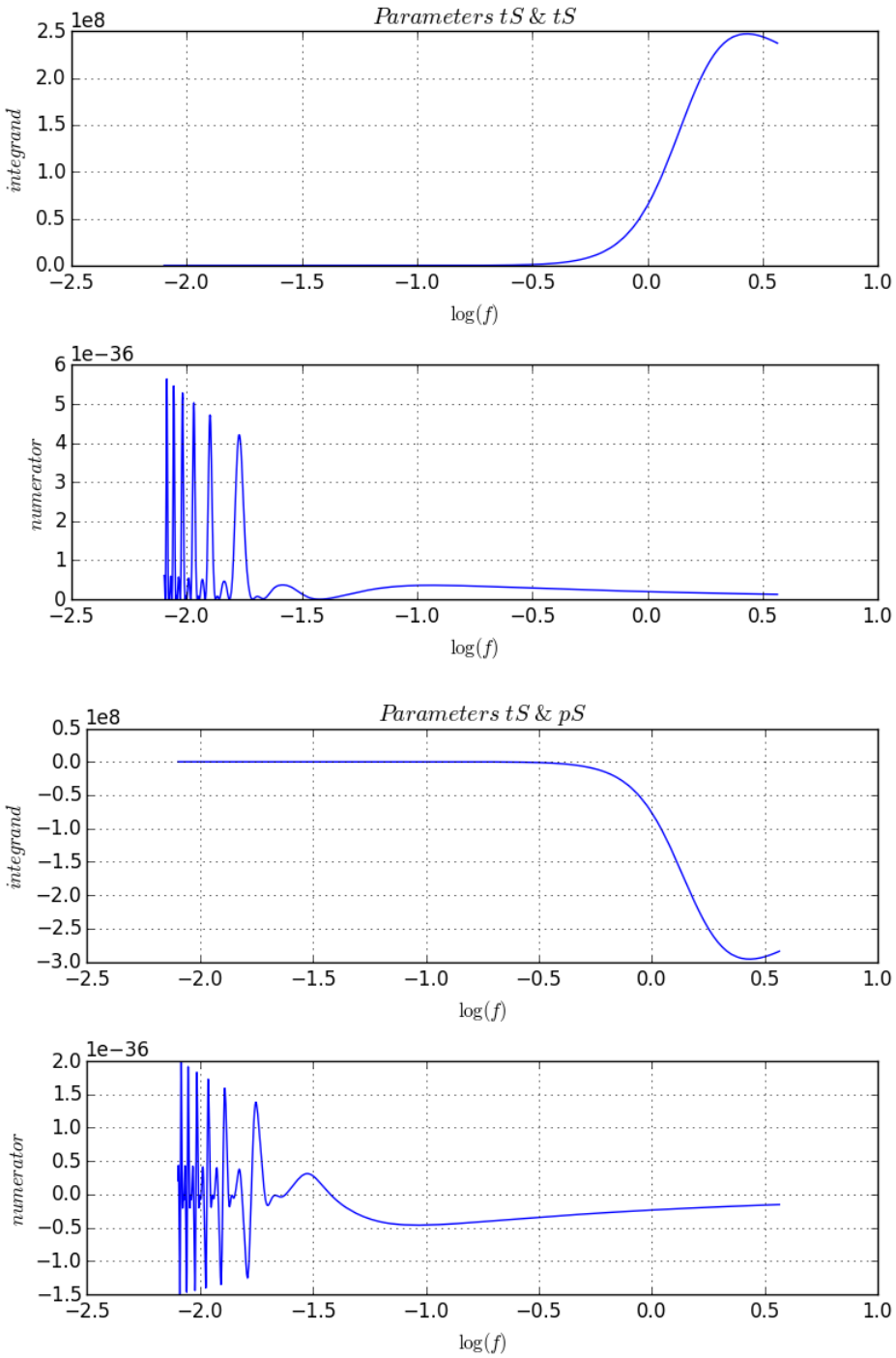
Parameters tS & tS
1e8
integrand
log(f)
1e−36
numerator
log(f)
Parameters tS & pS
1e8
integrand
log(f)
1e−36
numerator
log(f)

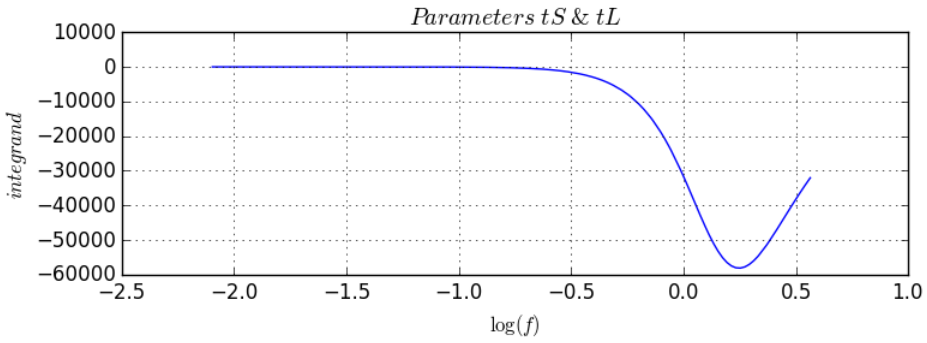
Parameters tS & tL
integrand
log(f)

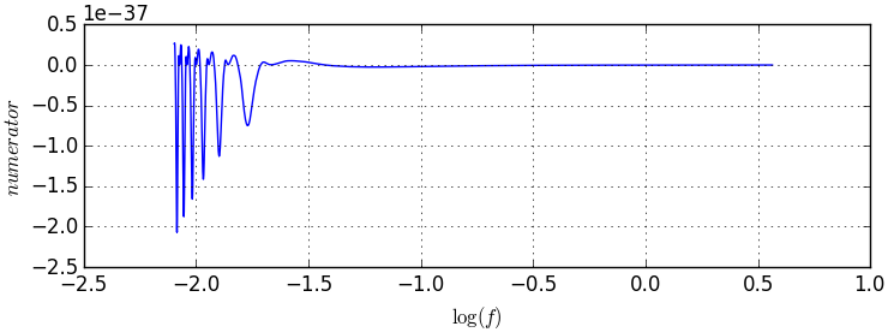
1e−37
numerator
log(f)

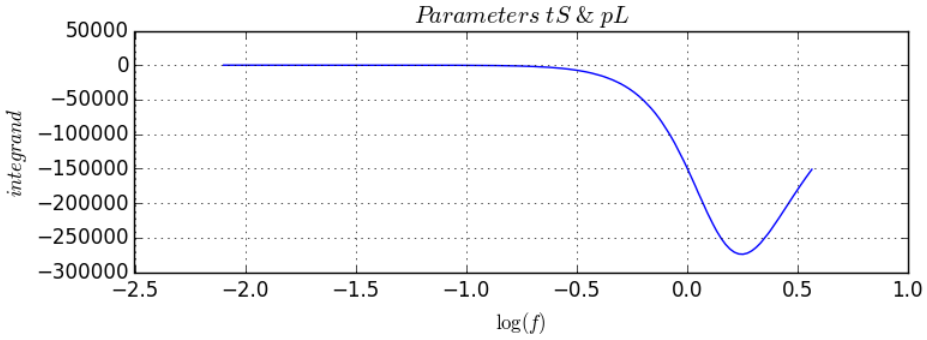
Parameters tS & pL
integrand
log(f)

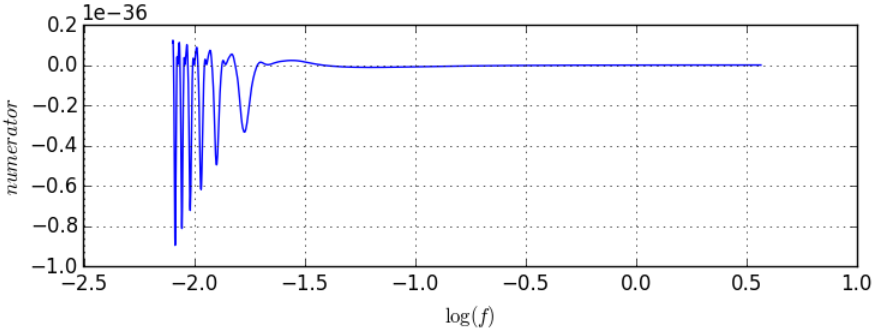
1e−36
numerator
log(f)

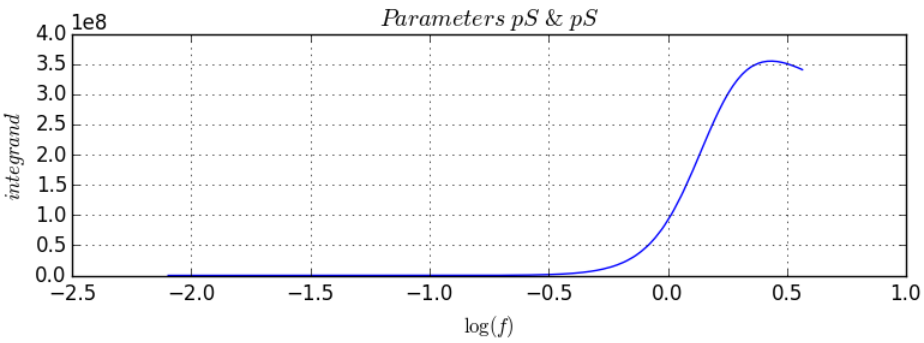
Parameters pS & pS
1e8
integrand
log(f)

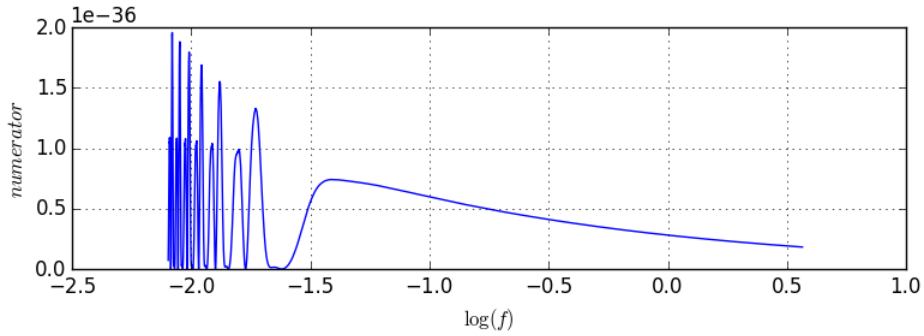
1e−36
numerator
log(f)

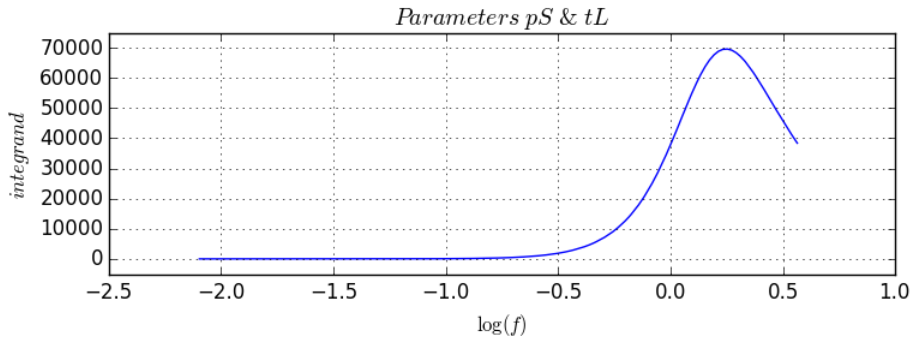
Parameters pS & tL
integrand
log(f)

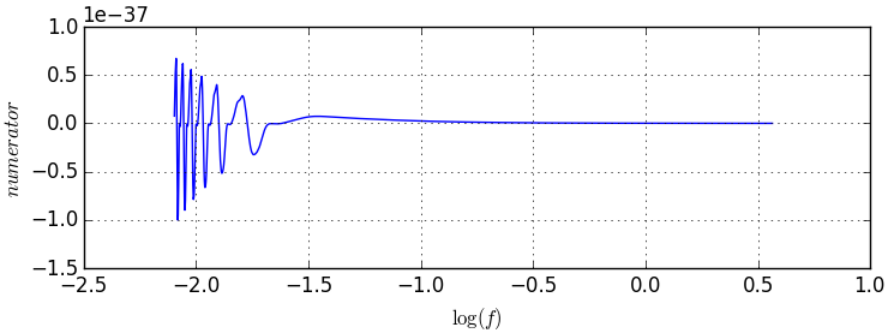
1e−37
numerator
log(f)

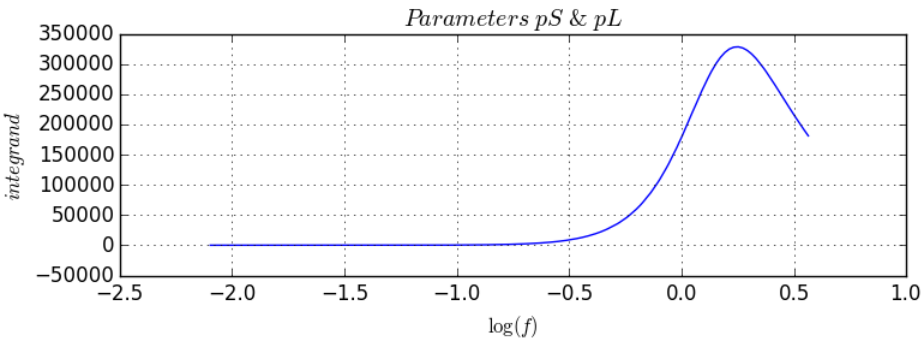
Parameters pS & pL
integrand
log(f)

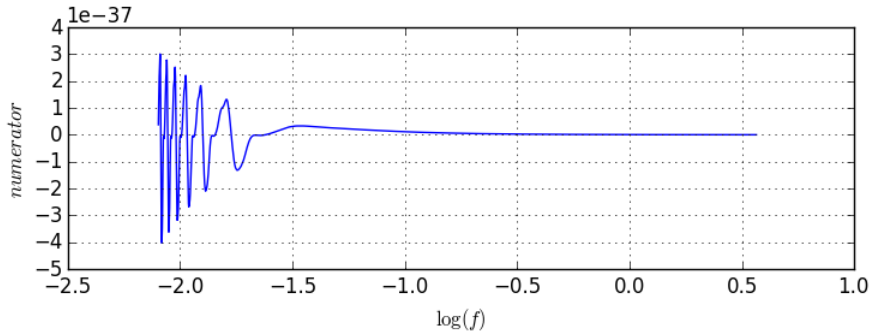
1e−37
numerator
log(f)

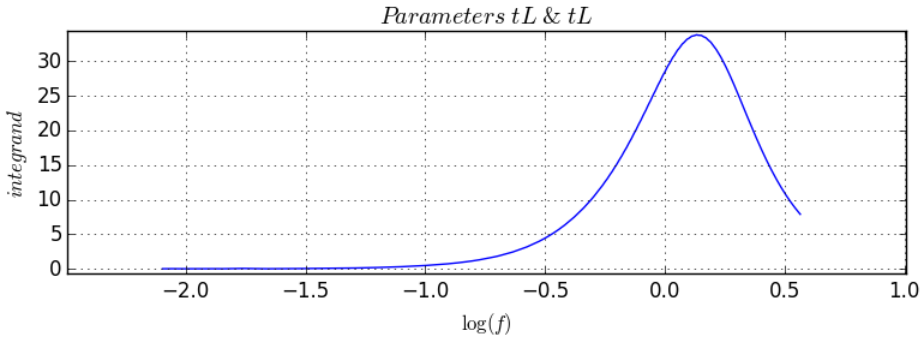
Parameters tL & tL
integrand
log(f)

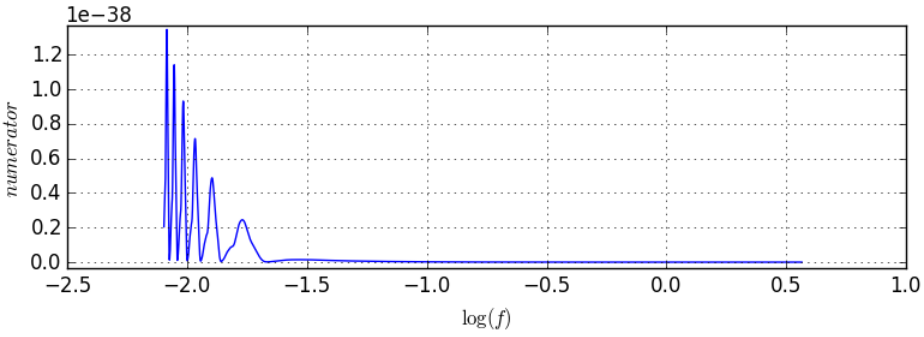
1e−38
numerator
log(f)

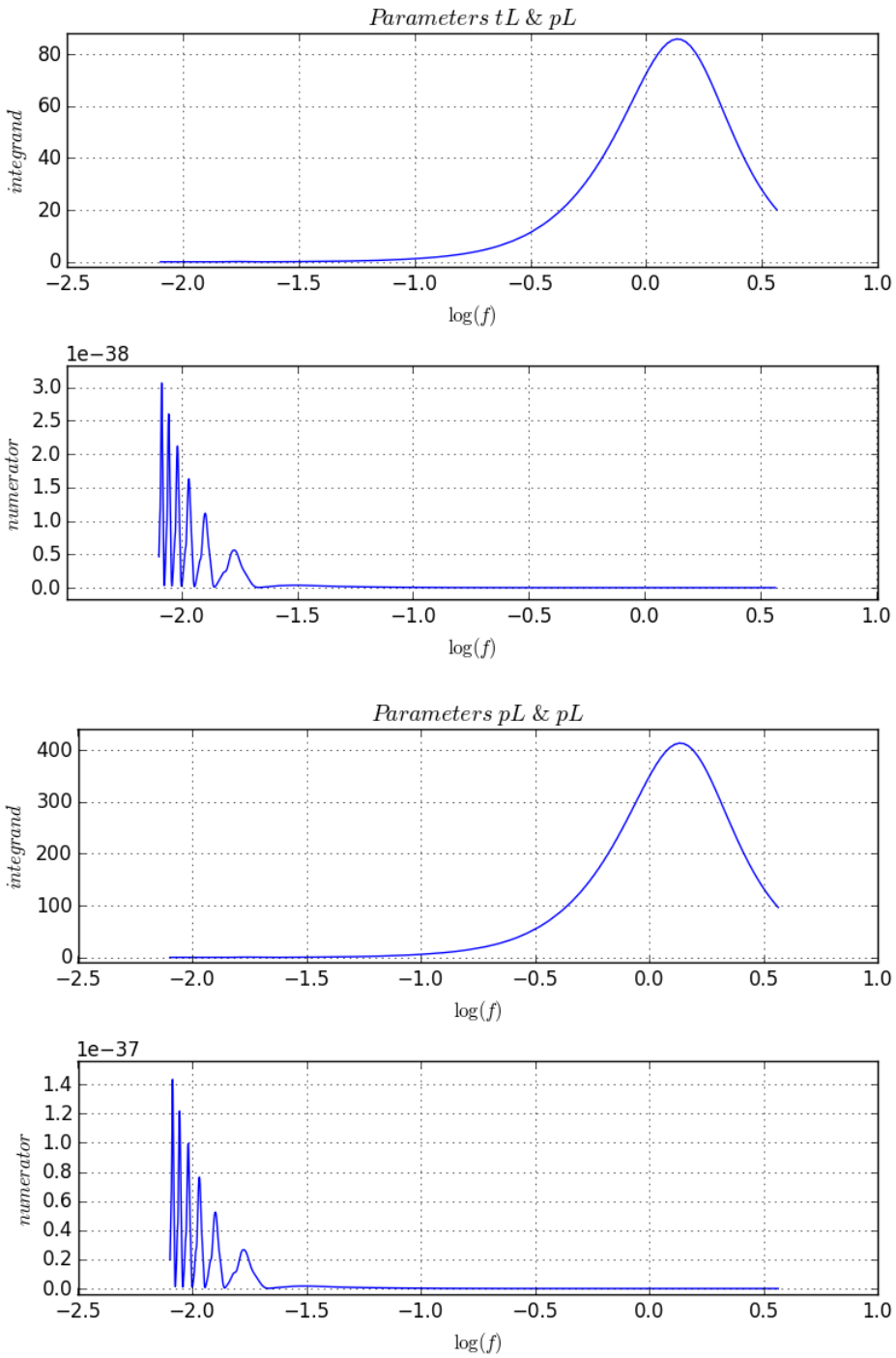
Parameters tL & pL
integrand
log(f)
1e−38
numerator
log(f)
Parameters pL & pL
integrand
log(f)
1e−37
numerator
log(f)

Figure 14: Waveform^2 for a 150/50 $M_\odot$ binary black hole system at arbitrary angle, over the detector's PSD. This is the integrand from the inner product in the SNR calculation.

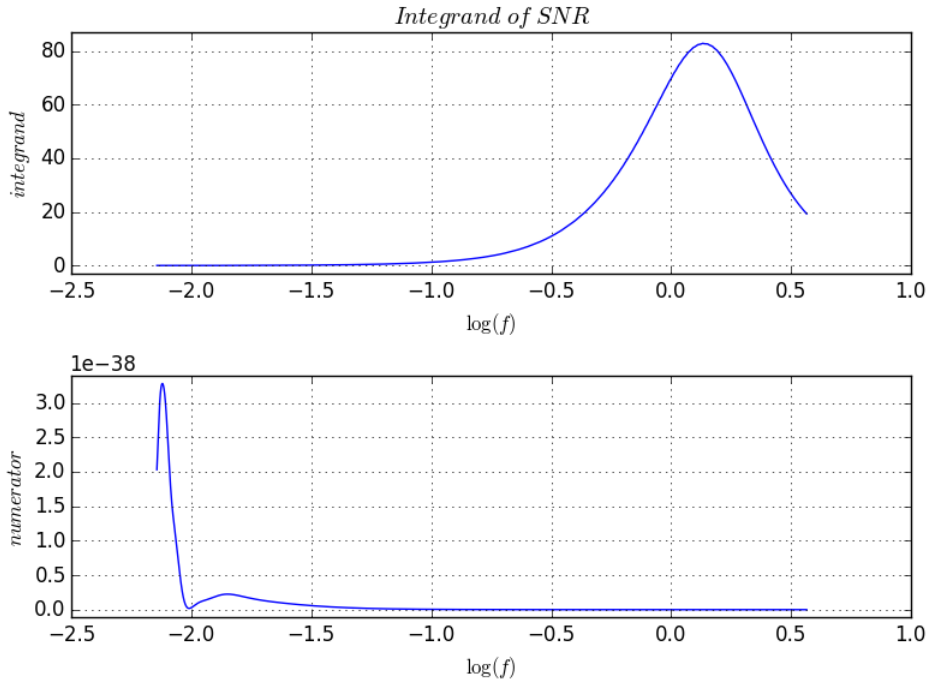

References

[1] Leor Barack and Curt Cutler, *LISA Capture Sources: Approximate Waveforms, Signal-to-Noise Ratios, and Parameter Estimation Accuracy*. arXiv:gr-qc/0310125v3 (2004).

[2] Curt Cutler, *Angular Resolution of the LISA Gravitational Wave Detector*. Physical Review D 57, 12 (1998).

[3] Curt Cutler and Eanna E Flanagan, *Gravitational waves from merging compact binaries: How accurately can one extract the binary's parameters from the inspiral waveform?*. Physical Review D 49, 6 (1994).

[4] Curt Cutler and Jan Harms, *BBO and the Neutron-Star-Binary Subtraction Problem*. arXiv:gr-qc/0511092v4 (2006).

[5] Curt Cutler and Daniel E. Holz, *Ultra-high precision cosmology from gravitational waves*. arXiv:0906.3752 (2009).

[6] Curt Cutler and Michele Vallisneri, *LISA detections of massive black hole inspirals: Parameter extraction errors due to inaccurate template waveforms*. Physical Review D 76, 104018 (2007).

[7] Eanna E Flanagan and Scott A Hughes, *The basics of gravitational wave theory*. New Journal f Physics, 7(1) (2005).

[8] Scott A Hughes, *Listening to the universe with gravitational-wave astronomy*. Annals of Physics, 303(1):142-178, (2002).

[9] Michele Maggiore, *Gravitational Waves: Volume 1 Theory and Experiments*. Oxford University Press, New York, 554, (2002).

[10] Christopher Moore, Robert Cole and Christopher Berry, *Gravitational Wave Sensitivity Curve*. http://rhcole.com/apps/GWplotter/

[11] B.S. Sathyaprakash, B.F. Schutz, and C. Van Den Broeck, *Cosmography with the Einstein Telescope*. arXiv:0906.4151v1 (2009).

[12] Correspondence with Dr. Rana Adhikari, Tom Callister.